Star formation in different environments

樋口, 公紀

https://doi.org/10.15017/4059984

出版情報：九州大学, 2019, 博士（理学）, 課程博士
バージョン：
権利関係：

Star formation in different environments

HIGUCHI Koki

Department of Earth and Planetary Sciences,

Graduate School of Science, Kyushu University

February 2020

Abstract

The environment in which stars are formed varies depending on the location and time of the galaxy. Furthermore, stars are closely related to the formation of galaxies and the chemical evolution of the universe. Therefore, in order to understand the history of the universe, it is necessary to clarify the star formation process. The evolution of collapsing clouds embedded in different environments is investigated using three-dimensional non-ideal magnetohydrodynamics simulations considering different metallicities ($Z/Z_{\odot}$) and ionization strengths (C_{ζ}, where C_{ζ} is a coefficient controlling the ionization intensity). I consider 32 different star-forming environments in combination with $Z = 0,\ 10^{-7},\ 10^{-6},\ 10^{-5},\ 10^{-4},\ 10^{-3},\ 10^{-2},\ 10^{-1}\ Z_{\odot}$ and $C_{\zeta} = 0,\ 0.01,\ 1,\ 10$, and prepare clouds having different the mass-to-flux ratio μ_0 and the ratio of rotational energy to gravitational energy β_0. I investigate the fragmentation condition in various star-forming environments. I perform 334 runs in total and it is found that 71 models show fragmentation and 15 models show a spiral structure. This study indicates that fragmentation tend to occur with high ionization strength, high metallicity, high μ_0 ($\mu_0 \geq 10$, where μ_0 means the mass-to-flux ratio normalized by the critical value), and high β_0 ($\beta_0 \geq 3.0 \times 10^{-2}$). In the collapsing cloud, fragmentation occurs when the following conditions are fulfilled; the high oblateness of core $\epsilon_{ob} \geq 5$, $\mu \geq 0.6 - 1.0$, and $\beta \geq 1.0 \times 10^{-2}$. There are some non-fragmentation cases with high μ_0 and β_0. These models are likely to show fragmentation in the later phase. A closed binary system should appear in such models. Furthermore, if these binaries gain a lot of mass and grow into a massive star binary, it can be the origin of the binary black hole.

Contents

Chapter 1

INTRODUCTION

1.1 Star-forming environments

There are various star-forming environments in the universe. Within the first billion years after the Big Bang ($z \sim 9-11$), about 40 galaxy candidates have been detected (e.g., Bouwens et al. 2011, Coe et al. 2013, Ellis et al. 2013, Bouwens et al. 2016, Oesch et al. 2016, Lam et al. 2019). These star-forming environments are likely to be the second generation star formation sites. Fig.1.1 shows the promising $z > 8.5$ candidate discovered using *Hubble Space Telescope*. With the improvement of the accuracy of telescopes, many distant candidate objects have been found. For galaxies with $z \geq 6$, these number is more than 800 (e.g., McLure et al. 2013, Bouwens et al. 2015). These high-redshift galaxies are thought to play an important role in the reionization of the universe (e.g., Stanway et al. 2003, Ishigaki et al. 2015). Starburst galaxies at $z \sim 2$ are the most active star formation environment in the universe (e.g., Steidel et al. 1996, 2004, Tacconi et al. 2008) The star-formation rates (SFR) of them exceed 100 solar masses per year, and for example, NAv1.144 galaxy has SFR $\sim 1338\,M_{\odot}\mathrm{yr}^{-1}$, its star-forming activity is very high (Falgarone et al. 2017). In such a diverse environment, various star formation processes are expected. Because the cloud differs depending on the surrounding characteristics, the characteristics of the protostar that is finally formed in should be also different.

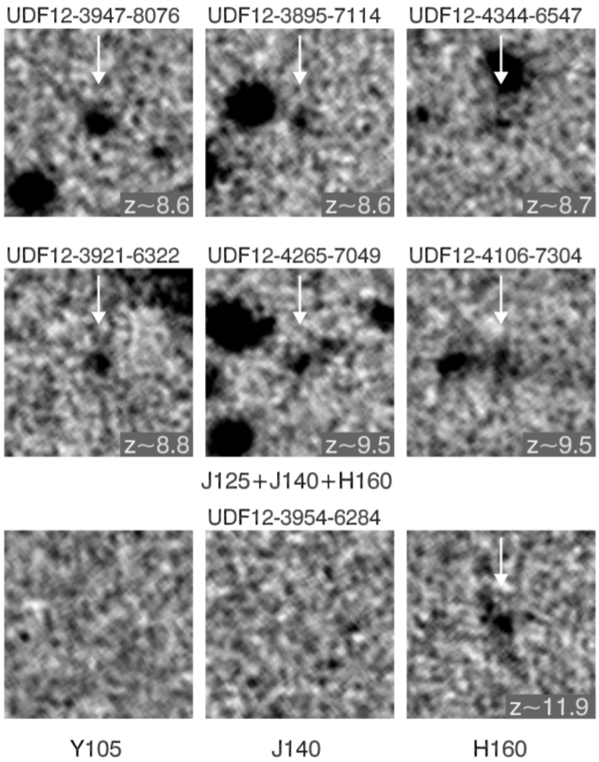

Figure 1.1: *Hubble Space Telescope* WFC3/IR images of the promising $z > 8.5$ candidates (Ellis et al. 2013).

1.2 First star v.s. Present-day stars

The first star, that is formed from pristine gas at epoch of cosmic dawn ($z \sim 30$), is expected to be more massive ($M \sim 10 - 1000\,M_{\odot}$; see Fig.1.2) than the present-day star (the typical mass is $\leq 1\,M_{\odot}$) (Hirano et al. 2014, 2015). The primordial gas has a high temperature due to the lack of coolant (e.g., heavier element and dust). As a result, because of the high gas temperature which is about two orders of magnitude higher than the present-day temperature, the Jeans mass is large. Thus, the typical mass of the first star is assumed to be higher than the nearby stars (e.g., Abel et al. 2002, Bromm et al. 2002). The difference in the stellar mass affects the radiation intensity, thus change the thermal and chemical evolution of the next-generation star-formation site (e.g., Hosokawa et al. 2011, 2012, 2016, Susa et al. 2014). It is important to accurately estimate the mass and multiplicity.

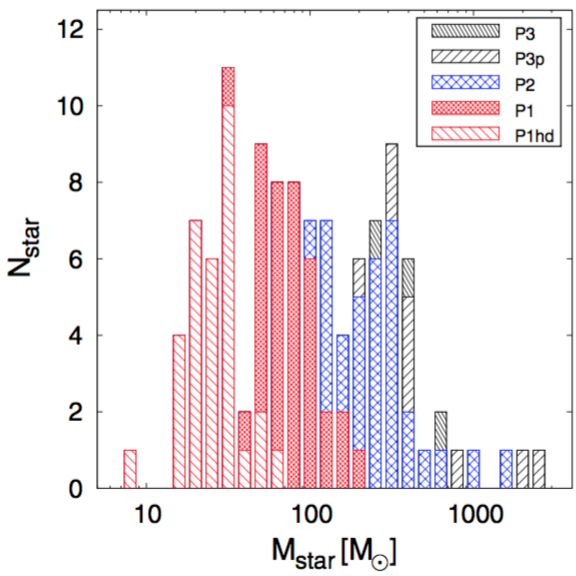

Figure 1.2: Final distribution of the calculated stellar masses for first stars (Hirano et al. 2014). The horizontal axis indicates the mass of stars, and the vertical axis indicates the number. The difference in color represents the difference in protostellar evolution.

1.3 Cloud fragmentation

One important issue is the stellar multiplicity. When fragmentation occurs in a cloud, the stellar mass greatly changes. Dynamical, radiative and chemical feedbacks to the surroundings are roughly limited by the stellar mass (e.g., Baraffe et al. 2001, Heger and Woosley 2002, Latif and Khochfar 2019). When a star that is predicted to have a large mass, such as the first star, is formed as a binary, the possibility of progenitors of gamma-ray bursts and gravitational wave sources (e.g., Kinugawa et al. 2017) becomes high, which is very important.

Recent numerical simulations of the first star (Pop. III star) have mentioned the possibility of fragmentation. Turk et al. (2009) performed hydrodynamical simulations that start from cosmological initial conditions. They simulated five realization of the first generation of Population III stars (Pop. III.1 stars) and found fragmentation in primordial gas cloud with rotation and turbulence. Pop. III.1 star is formed in pristine clouds unaffected by prior star formation. Clark et al. (2011) explored the effects of turbulence on the Pop. III.1 and Pop. III.2 star formation. Pop. III.2 star is formed

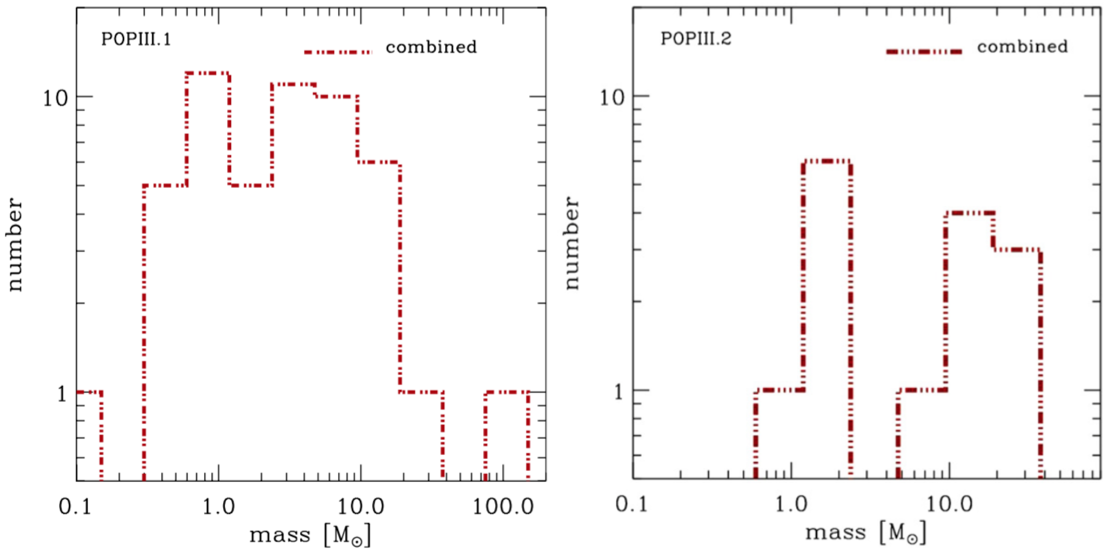

Figure 1.3: The mass function of Pop. III.1 (left panel) and Pop. III.2 star (right panel) for their simulations (Clark et al. 2011).

in clouds having a high ionization fraction. Pop. III.1 star is easier to fragment than Pop. III.2 star (see Fig.1.3), because there is an adiabatic phase (at $n \sim 10^7\,\mathrm{cm}^{-3}$) in Pop. III.2 star formation. Machida et al. (2008a) performed MHD simulations including self-gravity, and indicated that core fragments in the range of $\beta_0 > 10^6$ during the collapse (see Fig.1.4). In addition, Machida et al. (2008b) examined that fragmentation processes in a collapsing primordial cloud using three-dimensional MHD simulations. They showed that fragmentation occurs before protostar formation with $\Omega_c > 10^{-17}(n_c/10^3\,\mathrm{cm}^{-3})^{2/3}\mathrm{s}^{-1}$ and $\beta_0 > \gamma_0$. As can be seen, the presence of a magnetic field and rotation greatly changes the picture of star formation (Fig.1.4). In particular, the magnetic field causes magnetic breaking (e.g., Basu and Mouschovias 1994) and outflow (e.g., Tomisaka 2000, Banerjee and Pudritz 2006, Machida et al. 2007, Tomida et al. 2015), and plays an important role for angular momentum transfer in the present-day star formation process.

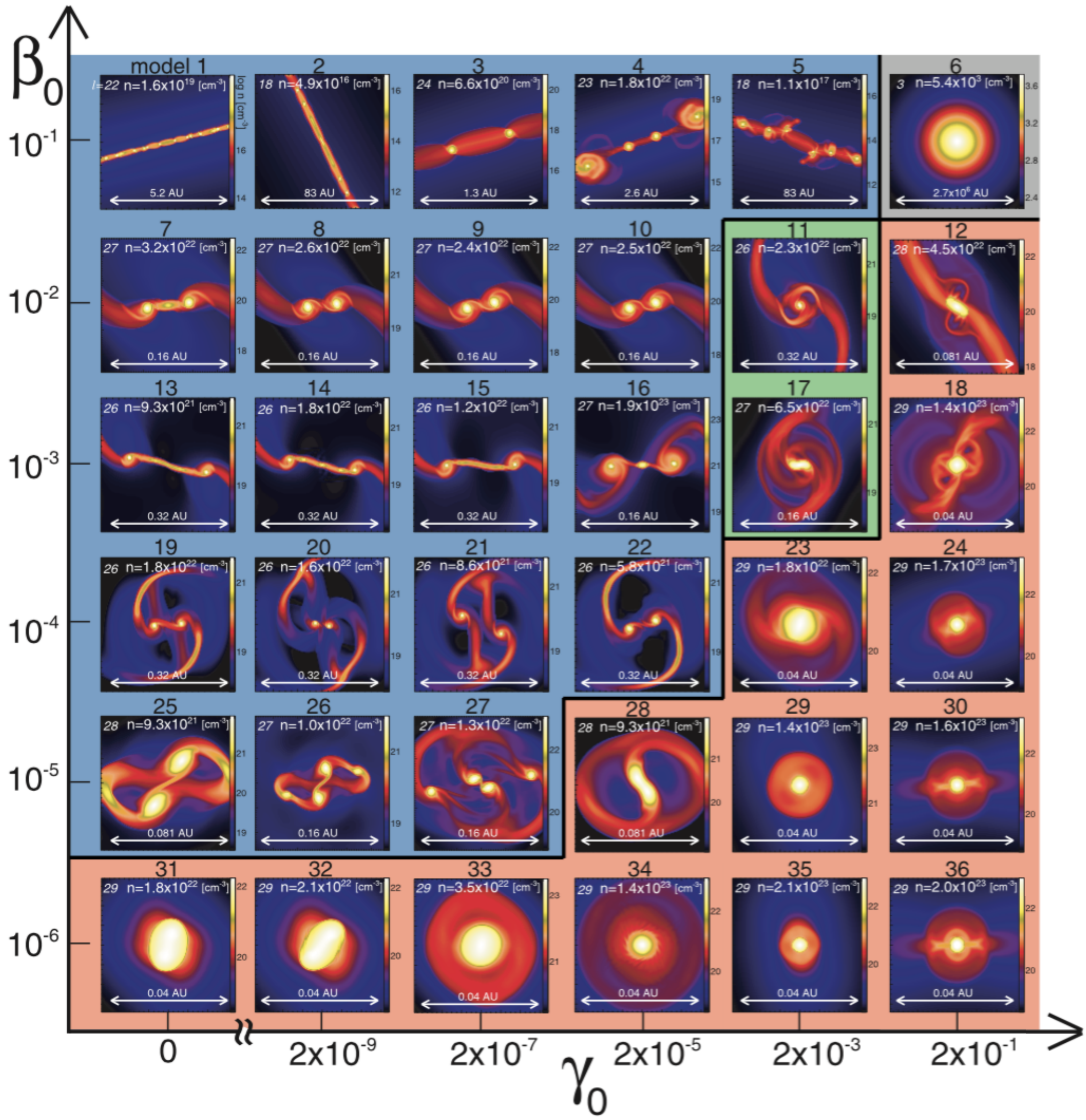

Figure 1.4: Simulation result for Machida et al. (2008a). Plots of density distribution of each model with models arranged based on the ratio of rotational energy to gravitational energy β_0 (vertical axis) and the ratio of magnetic energy to gravitational energy γ_0 (horizontal axis).

1.4 Observations in the present-day star-forming region

1.4.1 Magnetic field

Magnetic fields play a vital role in the physics of interstellar medium. The magnetic field strength is measured using the Zeeman effect. In our galaxy, the star-forming clouds have smaller μ, which is the mass-to-flux ratio of the initial cloud normalized

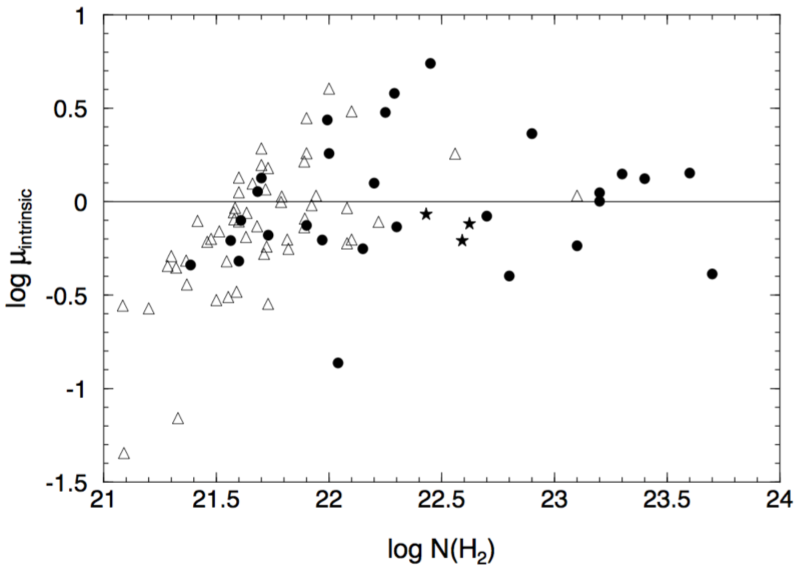

Figure 1.5: The observed mass-to-flux ratios for star-forming clouds (Heiles and Crutcher 2005).

by the critical value,

$$\mu_0 = \frac{(M/\Phi)}{(M/\Phi)_{\rm cri}}, \tag{1.1}$$

where M and Φ are the mass and magnetic flux of the initial cloud, respectively, and $(M/\Phi)_{\rm cri}$ is the ratio of the critical values of these parameters, which is $(M/\Phi)_{\rm cri} \equiv (2\pi G^{1/2})^{-1}$ (Nakano and Nakamura 1978). Observation shows that $\mu \leq 10$ (Crutcher 1999, Heiles and Crutcher 2005, Crutcher et al. 2010: see also Fig.1.5). It is shown that the $B_{\rm max}$ of the molecular cloud in the vicinity is proportional to the 2/3 power of $n\,{\rm cm}^{-3}$ in the range of $n > 300\,{\rm cm}^{-3}$, for example, in molecular cloud cores, $B_{\rm max}$ is a few 10 μG. On the other hand, since the magnetic field is amplified with the formation of the cosmic structure and the evolution of the star, the higher red-shifted star-forming environment, a field strength becomes weak. Mao et al. (2017) detected coherent μG magnetic fields in the foreground galaxy at $z = 0.439$. The strength of the magnetic field in the early universe is very weak, less than 1nG, but it is suggested that the magnetic field is locally amplified to about μG as the structure is formed (e.g., Schleicher et al. 2010, Susa et al. 2015). It is comparable to thermal energy and turbulent energy, and magnetic field could be dynamically important.

1.4.2 Multiplicity

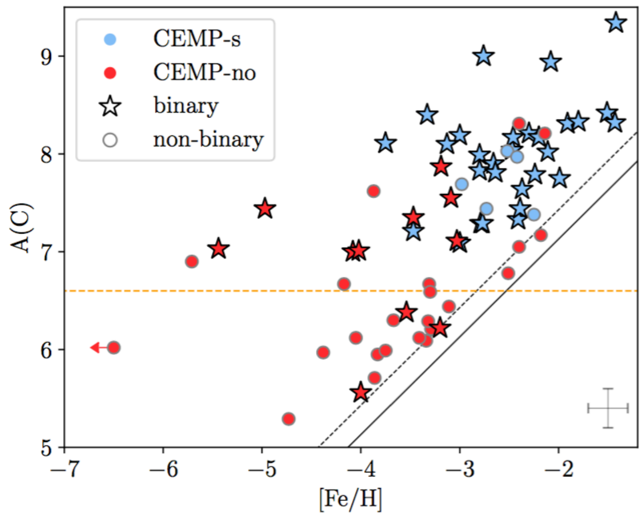

Figure 1.6: Carbon abundance for CEMP stars (Arentsen et al. 2019).

The characteristics of stars in our galaxy and others has been investigated through observational studies. Dense molecular cloud cores are initially rotating with rates of $\beta \leq 0.15$ with a mean value of $\beta \sim 0.02$ (Goodman et al. 1993), where β is the parameter defined as the ratio of rotational kinetic energy to gravitational energy, and $\beta \sim 0.02$ indicates that rotation is energetically dominant in the support of the cloud core. In fact, 60 to 80% of the field stars in the galaxy are suggested as binary stars (Duquennoy and Mayor 1991), and it seems that the rotation has an important influence on star formation. On the other hands, when metal-poor stars are observed, these stars are found as carbon-enhanced metal-poor (CEMP) stars. There are two types of CEMP stars, which are CEMP-s and CEMP-no stars, initially defined by Beers and Christlieb (2005). The CEMP-s stars show additional enhancements to the s-process element, while the CEMP-no stars do not show this trend. CEMP-s stars are observed as binary with almost 100% probability (e.g., McClure and Woodsworth 1990, Lucatello et al. 2005). CEMP-no stars are observed as binary with higher absolute carbon abundance with a proportion of 47% and lower absolute carbon content with a probability 18% (Arentsen et al. 2019). Fig.1.6 shows the Carbon abundance for CEMP stars with respect to the $Z/Z_{\odot}$, and there is a tendency that binary is decreasing as the metallicity decreases. It is necessary to simulate whether this tendency is real.

Chapter 2

METHODS

2.1 Parameters

I prepare 32 environments characterized by metallicity $Z/Z_\odot$ and ionization parameter C_ζ. I consider the metallicity in the range of $0 \leq Z/Z_\odot \leq 10^{-1}$ ($Z/Z_\odot = 0$, 10^{-7}, 10^{-6}, 10^{-5}, 10^{-4}, 10^{-3}, 10^{-2}, 10^{-1}). The ionization strength is defined as

$$\zeta = \zeta_{\rm CR} + \zeta_{\rm RE,short} + \zeta_{\rm RE,long}, \tag{2.1}$$

$$\zeta_{\rm CR} = C_\zeta \, \zeta_{\rm CR,0} \exp(-\rho {\rm R_J}/\lambda), \tag{2.2}$$

$$\zeta_{\rm RE,short} = 7.6 \times 10^{-19} {\rm s^{-1}} \, {\rm C}_\zeta, \tag{2.3}$$

and

$$\zeta_{\rm RE,long} = 1.4 \times 10^{-22} {\rm s^{-1}} \, {\rm Z/Z_\odot}. \tag{2.4}$$

Eqs.2.2–2.4 show the contribution of cosmic rays, short-lived, and long-lived radioactive elements, respectively. $\zeta_{\rm CR,0}$ ($= 1 \times 10^{-17}\,{\rm s^{-1}}$), $R_{\rm J}$ and λ ($= 96\,{\rm g\,cm^{-2}}$) mean the cosmic-ray ionization rate in the local interstellar medium, the Jeans length and attenuation length, respectively (Susa et al. 2015, Higuchi et al. 2018). C_ζ is a parameter representing the ionization strength of $\zeta_{\rm CR}$ and $\zeta_{\rm RE,short}$. $C_\zeta = 1$ is defined in the nearby star-forming environment, and $C_\zeta = 0.01$ or 10 are adjusted to an ionization intensity corresponding to the first galaxy like or starburst galaxy like environment. When $C_\zeta = 0$, the contribution of cosmic ray and short-lived radioactive elements disappears (in eqs.2.2 and 2.3). In addition, when metallicity becomes zero, the contribution of long-lived radioactive elements also disappears (in eq.2.4), which corresponds to the primitive environment at the beginning of the universe (for details, see Susa et al. 2015). Combining two parameters, which are the metallicity ($Z/Z_{\odot} = 0$, 10^{-7}, 10^{-6}, 10^{-5}, 10^{-4}, 10^{-3}, 10^{-2}, 10^{-1}) and the ionization parameter ($C_{\zeta} = 0$, 0.01, 1, and 10), I investigate 32 collapsing gas clouds embedded in various environments. The model names and physical quantities of each cloud are listed in the Table 2.1–2.4.

2.2 Numerical method and basic equations

As the initial state of star-forming clouds, a critical Bonnor – Ebert (B.E.) density profile (Ebert 1955, Bonnor 1956), which is usually used as the initial condition of cloud (e.g., Matsumoto and Tomisaka 2004, Banerjee and Pudritz 2006), is adopted for each model. This density profile is determined by the central number density n_c and the cloud temperature $T_{\rm cl}$. $T_{\rm cl}$ is determined as the one-zone calculation of the thermal/chemical evolution with different metallicity and ionization strength, and the initial central number density is adopted as $n_{c,0} = 10^4\,{\rm cm}^{-3}$. Details are described in Table 2.1–2.4. To promote contraction, the density is set to 1.8 times the critical B.E. density profile (Machida and Hosokawa 2013, Higuchi et al. 2018, 2019). Clouds have initially different radii and masses with different models (for specific value, see Table 2.1–2.4), but the ratio of thermal to gravitational energy α_0, which greatly affects cloud collapse, is the same value ($\alpha = 0.47$) for all models. In this study, simulation is performed with different ratio of rotational to gravitational energy β_0 and mass-to-flux ratio μ_0 of the initial cloud in order to investigate the fragmentation process of the 32 collapsing cloud (Tabele 2.1–2.4).

The cloud collapse for each model in Table 2.1–2.4 is calculated using three-dimensional non-ideal MHD nested grid simulations in the same way as Higuchi et al. (2018, 2019).

The following basic equations are implemented in the nested grid code:

$$\frac{\partial \rho}{\partial t} + \nabla \cdot (\rho \boldsymbol{v}) = 0, \tag{2.5}$$

$$\rho \frac{\partial \boldsymbol{v}}{\partial t} + \rho (\boldsymbol{v} \cdot \nabla) \boldsymbol{v} = -\nabla P - \frac{1}{4\pi} \boldsymbol{B} \times (\nabla \times \boldsymbol{B}) - \rho \nabla \phi, \tag{2.6}$$

$$\frac{\partial \boldsymbol{B}}{\partial t} = \nabla \times \left[\boldsymbol{v} \times \boldsymbol{B} + \frac{\eta_{\rm AD}}{|\boldsymbol{B}|^2} [(\nabla \times \boldsymbol{B}) \times \boldsymbol{B}] \times \boldsymbol{B} - \eta_{\rm OD} (\nabla \times \boldsymbol{B}) \right], \tag{2.7}$$

$$\nabla^2 \phi = 4\pi G \rho, \tag{2.8}$$

where ρ, $\boldsymbol{v}$, P, $\boldsymbol{B}$, and ϕ denote the density, velocity, pressure, magnetic flux density, and gravitational potential, respectively. The gas pressure P is taken from the table calculated by the one-zone calculation (for details, see Higuchi et al. 2018, 2019). The coefficients of Ohmic resistivity $\eta_{\rm OD}$ and ambipolar diffusion $\eta_{\rm AD}$ are also obtained from the table. Note that $\eta_{\rm OD}$ is referenced from the table as the density argument, while $\eta_{\rm AD}$ is referenced as both density and magnetic field strength arguments (Susa et al. 2015, Higuchi et al. 2018). Each grid is composed of (i, j, k) = (64, 64, 32), and mirror symmetry is applied with respect to the z-axis (for a detailed, see Machida et al. 2004, 2005, 2007, 2008a). The finer grid is embedded in the coarser grid and the finer grid is continuously generated so that the Jeans length is resolved at least 16 cells (Truelove et al. 1997). Using this code, the cloud evolution is calculated during collapsing phase ($n_c \leq 10^{16}\,{\rm cm}^{-3}$). I also examine the contribution of the ionization strength, the metallicity, the magnetic field, and rotation of cloud to fragmentation.

Table 2.1: Model parameters in the case of $C_\zeta = 0$. Columns 1 and 2 list the model number and model name, respectively. Columns 3 through 6 list the ionization strength C_ζ, the metallicity $Z/Z_\odot$, the ratio of rotational to gravitational energy β_0, and the mass-to-flux ratio μ_0, respectively. Columns 7 through 11 list the initial magnetic field strength B_0, the initial angular velocity Ω_0, the cloud mass $M_{\rm cl}$, the cloud temperature $T_{\rm cl}$, and the cloud radius $r_{\rm cl}$, respectively. Column 12 lists whether fragment ($\circ$) or spiral ($\diamond$) appear or not ($\times$).

	Model	C_ζ	$Z/Z_\odot$	μ_0	β_0	$B_0(\mu$G)	Ω_0(s^{-1})	$M_{\rm cl}(M_\odot)$	$T_{\rm cl}$(K)	$r_{\rm cl}$(au)	fragmentation
1	I0ZPM3R5			3	10^{-5}	34.1	3.05×10^{-16}				$\times$
2	I0ZPM3R3			3	10^{-3}	34.1	3.05×10^{-15}				$\times$
3	I0ZPM3R1			3	10^{-1}	34.1	3.05×10^{-14}				$\times$
4	I0ZPM5R5			5	10^{-5}	20.5	3.05×10^{-16}				$\times$
5	I0ZPM5R3	0	0	5	10^{-3}	20.5	3.05×10^{-15}	1.08×10^4	198	4.91×10^5	$\times$
6	I0ZPM5R1			5	10^{-1}	20.5	3.05×10^{-14}				$\times$
7	I0ZPM10R5			10	10^{-5}	10.2	3.05×10^{-16}				$\times$
8	I0ZPM10R3			10	10^{-3}	10.2	3.05×10^{-15}				$\times$
9	I0ZPM10R1			10	10^{-1}	10.2	3.05×10^{-14}				$\times$
10	I0Z7M3R5			3	10^{-5}	34.1	3.05×10^{-16}				$\times$
11	I0Z7M3R3			3	10^{-3}	34.1	3.05×10^{-15}				$\times$
12	I0Z7M3R1			3	10^{-1}	34.1	3.05×10^{-14}				$\times$
13	I0Z7M5R5			5	10^{-5}	20.5	3.05×10^{-16}				$\times$
14	I0Z7M5R3	0	10^{-7}	5	10^{-3}	20.5	3.05×10^{-15}	1.08×10^4	198	4.91×10^5	$\times$
15	I0Z7M5R1			5	10^{-1}	20.5	3.05×10^{-14}				$\times$
16	I0Z7M10R5			10	10^{-5}	10.2	3.05×10^{-16}				$\times$
17	I0Z7M10R3			10	10^{-3}	10.2	3.05×10^{-15}				$\times$
18	I0Z7M10R1			10	10^{-1}	10.2	3.05×10^{-14}				$\times$
19	I0Z6M3R5			3	10^{-5}	34.1	3.05×10^{-16}				$\times$
20	I0Z6M3R3			3	10^{-3}	34.1	3.05×10^{-15}				$\times$
21	I0Z6M3R1			3	10^{-1}	34.1	3.05×10^{-14}				$\times$
22	I0Z6M5R5			5	10^{-5}	20.5	3.05×10^{-16}				$\times$
23	I0Z6M5R3	0	10^{-6}	5	10^{-3}	20.5	3.05×10^{-15}	1.07×10^4	198	4.91×10^5	$\times$
24	I0Z6M5R1			5	10^{-1}	20.5	3.05×10^{-14}				$\times$
25	I0Z6M10R5			10	10^{-5}	10.2	3.05×10^{-16}				$\times$
26	I0Z6M10R3			10	10^{-3}	10.2	3.05×10^{-15}				$\times$
27	I0Z6M10R1			10	10^{-1}	10.2	3.05×10^{-14}				$\times$
28	I0Z5M3R5			3	10^{-5}	33.8	3.05×10^{-16}				$\times$
29	I0Z5M3R3			3	10^{-3}	33.8	3.05×10^{-15}				$\times$
30	I0Z5M3R1			3	10^{-1}	33.8	3.05×10^{-14}				$\times$
31	I0Z5M5R5			5	10^{-5}	20.3	3.05×10^{-16}				$\times$
32	I0Z5M5R3	0	10^{-5}	5	10^{-3}	20.3	3.05×10^{-15}	1.05×10^4	194	4.87×10^5	$\times$
33	I0Z5M5R1			5	10^{-1}	20.3	3.05×10^{-14}				$\times$
34	I0Z5M10R5			10	10^{-5}	10.1	3.05×10^{-16}				$\times$
35	I0Z5M10R3			10	10^{-3}	10.1	3.05×10^{-15}				$\times$
36	I0Z5M10R1			10	10^{-1}	10.1	3.05×10^{-14}				$\times$
37	I0Z4M3R5			3	10^{-5}	31.9	3.05×10^{-16}				$\times$
38	I0Z4M3R3			3	10^{-3}	31.9	3.05×10^{-15}				$\times$
39	I0Z4M3R1			3	10^{-1}	31.9	3.05×10^{-14}				$\diamond$
40	I0Z4M5R5			5	10^{-5}	19.1	3.05×10^{-16}				$\times$
41	I0Z4M5R3	0	10^{-4}	5	10^{-3}	19.1	3.05×10^{-15}	8.75×10^3	172	4.59×10^5	$\times$
42	I0Z4M5R1			5	10^{-1}	19.1	3.05×10^{-14}				$\diamond$
43	I0Z4M10R5			10	10^{-5}	9.56	3.05×10^{-16}				$\times$
44	I0Z4M10R3			10	10^{-3}	9.56	3.05×10^{-15}				$\times$
45	I0Z4M10R1			10	10^{-1}	9.56	3.05×10^{-14}				$\circ$
46	I0Z3M3R5			3	10^{-5}	24.6	3.06×10^{-16}				$\times$
47	I0Z3M3R3			3	10^{-3}	24.6	3.06×10^{-15}				$\times$
48	I0Z3M3R1			3	10^{-1}	24.6	3.06×10^{-14}				$\diamond$
49	I0Z3M5R5			5	10^{-5}	14.7	3.06×10^{-16}				$\times$
50	I0Z3M5R3	0	10^{-3}	5	10^{-3}	14.7	3.06×10^{-15}	3.98×10^3	103	3.52×10^5	$\times$
51	I0Z3M5R1			5	10^{-1}	14.7	3.06×10^{-14}				$\diamond$
52	I0Z3M10R5			10	10^{-5}	7.37	3.06×10^{-16}				$\times$
53	I0Z3M10R3			10	10^{-3}	7.37	3.06×10^{-15}				$\times$
54	I0Z3M10R1			10	10^{-1}	7.37	3.06×10^{-14}				$\diamond$
55	I0Z2M3R5			3	10^{-5}	9.83	3.15×10^{-16}				$\times$
56	I0Z2M3R3			3	10^{-3}	9.83	3.15×10^{-15}				$\times$
57	I0Z2M3R1			3	10^{-1}	9.83	3.15×10^{-14}				$\diamond$
58	I0Z2M5R5			5	10^{-5}	5.90	3.15×10^{-16}				$\times$
59	I0Z2M5R3	0	10^{-2}	5	10^{-3}	5.90	3.15×10^{-15}	2.27×10^2	16.4	1.33×10^5	$\times$
60	I0Z2M5R1			5	10^{-1}	5.90	3.15×10^{-14}				$\circ$
61	I0Z2M10R5			10	10^{-5}	2.95	3.15×10^{-16}				$\times$
62	I0Z2M10R3			10	10^{-3}	2.95	3.15×10^{-15}				$\times$
63	I0Z2M10R1			10	10^{-1}	2.95	3.15×10^{-14}				$\circ$
64	I0Z1M3R5			3	10^{-5}	10.3	3.78×10^{-16}				$\times$
65	I0Z1M3R3			3	10^{-3}	10.3	3.78×10^{-15}				$\times$
66	I0Z1M3R1			3	10^{-1}	10.3	3.78×10^{-14}				$\times$
67	I0Z1M5R5			5	10^{-5}	6.20	3.78×10^{-16}				$\times$
68	I0Z1M5R3	0	10^{-1}	5	10^{-3}	6.20	3.78×10^{-15}	1.26×10^2	18.1	9.67×10^4	$\times$
69	I0Z1M5R1			5	10^{-1}	6.20	3.78×10^{-14}				$\circ$
70	I0Z1M10R5			10	10^{-5}	3.10	3.78×10^{-16}				$\times$
71	I0Z1M10R3			10	10^{-3}	3.10	3.78×10^{-15}				$\circ$
72	I0Z1M10R1			10	10^{-1}	3.10	3.78×10^{-14}				$\circ$

Table 2.2: Same as Table 2.1, but moodel parameters in the case of $C_\zeta = 0.01$.

	Model	C_ζ	$Z/Z_\odot$	μ_0	β_0	$B_0(\mu\mathrm{G})$	$\Omega_0(\mathrm{s}^{-1})$	$M_{\mathrm{cl}}(M_\odot)$	T_{cl}(K)	r_{cl}(au)	fragmentation
73	I001ZPM3R5			3	10^{-5}	28.4	3.05×10^{-16}				×
74	I001ZPM3R3			3	10^{-3}	28.4	3.05×10^{-15}				×
75	I001ZPM3R1			3	10^{-1}	28.4	3.05×10^{-14}				×
76	I001ZPM5R5			5	10^{-5}	17.0	3.05×10^{-16}				×
77	I001ZPM5R3	0.01	0	5	10^{-3}	17.0	3.05×10^{-15}	6.20×10^{3}	137	4.09×10^{5}	×
78	I001ZPM5R1			5	10^{-1}	17.0	3.05×10^{-14}				○
79	I001ZPM10R5			10	10^{-5}	8.52	3.05×10^{-16}				×
80	I001ZPM10R3			10	10^{-3}	8.52	3.05×10^{-15}				×
81	I001ZPM10R1			10	10^{-1}	8.52	3.05×10^{-14}				○
82	I001Z7M3R5			3	10^{-5}	28.4	3.05×10^{-16}				×
83	I001Z7M3R3			3	10^{-3}	28.4	3.05×10^{-15}				×
84	I001Z7M3R1			3	10^{-1}	28.4	3.05×10^{-14}				○
85	I001Z7M5R5			5	10^{-5}	17.0	3.05×10^{-16}				×
86	I001Z7M5R3	0.01	10^{-7}	5	10^{-3}	17.0	3.05×10^{-15}	6.19×10^{3}	137	4.09×10^{5}	×
87	I001Z7M5R1			5	10^{-1}	17.0	3.05×10^{-14}				○
88	I001Z7M10R5			10	10^{-5}	8.52	3.05×10^{-16}				×
89	I001Z7M10R3			10	10^{-3}	8.52	3.05×10^{-15}				×
90	I001Z7M10R1			10	10^{-1}	8.52	3.05×10^{-14}				○
91	I001Z6M3R5			3	10^{-5}	28.4	3.05×10^{-16}				×
92	I001Z6M3R3			3	10^{-3}	28.4	3.05×10^{-15}				×
93	I001Z6M3R1			3	10^{-1}	28.4	3.05×10^{-14}				○
94	I001Z6M5R5			5	10^{-5}	17.0	3.05×10^{-16}				×
95	I001Z6M5R3	0.01	10^{-6}	5	10^{-3}	17.0	3.05×10^{-15}	6.18×10^{3}	137	4.08×10^{5}	×
96	I001Z6M5R1			5	10^{-1}	17.0	3.05×10^{-14}				○
97	I001Z6M10R5			10	10^{-5}	8.51	3.05×10^{-16}				×
98	I001Z6M10R3			10	10^{-3}	8.51	3.05×10^{-15}				×
99	I001Z6M10R1			10	10^{-1}	8.51	3.05×10^{-14}				○
100	I001Z5M3R5			3	10^{-5}	28.1	3.05×10^{-16}				×
101	I001Z5M3R3			3	10^{-3}	28.1	3.05×10^{-15}				×
102	I001Z5M3R1			3	10^{-1}	28.1	3.05×10^{-14}				○
103	I001Z5M5R5			5	10^{-5}	16.9	3.05×10^{-16}				×
104	I001Z5M5R3	0.01	10^{-5}	5	10^{-3}	16.9	3.05×10^{-15}	6.03×10^{3}	135	4.05×10^{5}	×
105	I001Z5M5R1			5	10^{-1}	16.9	3.05×10^{-14}				○
106	I001Z5M10R5			10	10^{-5}	8.44	3.05×10^{-16}				×
107	I001Z5M10R3			10	10^{-3}	8.44	3.05×10^{-15}				×
108	I001Z5M10R1			10	10^{-1}	8.44	3.05×10^{-14}				○
109	I001Z4M3R5			3	10^{-5}	26.2	3.05×10^{-16}				×
110	I001Z4M3R3			3	10^{-3}	26.2	3.05×10^{-15}				×
111	I001Z4M3R1			3	10^{-1}	26.2	3.05×10^{-14}				○
112	I001Z4M5R5			5	10^{-5}	15.7	3.05×10^{-16}				×
113	I001Z4M5R3	0.01	10^{-4}	5	10^{-3}	15.7	3.05×10^{-15}	4.88×10^{3}	117	3.77×10^{5}	×
114	I001Z4M5R1			5	10^{-1}	15.7	3.05×10^{-14}				○
115	I001Z4M10R5			10	10^{-5}	7.87	3.05×10^{-16}				×
116	I001Z4M10R3			10	10^{-3}	7.87	3.05×10^{-15}				×
117	I001Z4M10R1			10	10^{-1}	7.87	3.05×10^{-14}				○
118	I001Z3M3R5			3	10^{-5}	20.0	3.06×10^{-16}				×
119	I001Z3M3R3			3	10^{-3}	20.0	3.06×10^{-15}				×
120	I001Z3M3R1			3	10^{-1}	20.0	3.06×10^{-14}				○
121	I001Z3M5R5			5	10^{-5}	12.0	3.06×10^{-16}				×
122	I001Z3M5R3	0.01	10^{-3}	5	10^{-3}	12.0	3.06×10^{-15}	2.15×10^{3}	68.0	2.87×10^{5}	×
123	I001Z3M5R1			5	10^{-1}	12.0	3.06×10^{-14}				○
124	I001Z3M10R5			10	10^{-5}	6.00	3.06×10^{-16}				×
125	I001Z3M10R3			10	10^{-3}	6.00	3.06×10^{-15}				×
126	I001Z3M10R1			10	10^{-1}	6.00	3.06×10^{-14}				◇
127	I001Z2M3R5			3	10^{-5}	9.85	3.14×10^{-16}				×
128	I001Z2M3R3			3	10^{-3}	9.85	3.14×10^{-15}				×
129	I001Z2M3R1			3	10^{-1}	9.85	3.14×10^{-14}				○
130	I001Z2M5R5			5	10^{-5}	5.91	3.14×10^{-16}				×
131	I001Z2M5R3	0.01	10^{-2}	5	10^{-3}	5.91	3.14×10^{-15}	2.29×10^{2}	16.5	1.34×10^{5}	×
132	I001Z2M5R1			5	10^{-1}	5.91	3.14×10^{-14}				○
133	I001Z2M10R5			10	10^{-5}	2.95	3.14×10^{-16}				×
134	I001Z2M10R3			10	10^{-3}	2.95	3.14×10^{-15}				×
135	I001Z2M10R1			10	10^{-1}	2.95	3.14×10^{-14}				○
136	I001Z1M3R5			3	10^{-5}	10.4	3.78×10^{-16}				×
137	I001Z1M3R3			3	10^{-3}	10.4	3.78×10^{-15}				×
138	I001Z1M3R1			3	10^{-1}	10.4	3.78×10^{-14}				○
139	I001Z1M5R5			5	10^{-5}	6.21	3.78×10^{-16}				×
140	I001Z1M5R3	0.01	10^{-1}	5	10^{-3}	6.21	3.78×10^{-15}	1.28×10^{2}	18.2	9.72×10^{4}	×
141	I001Z1M5R1			5	10^{-1}	6.21	3.78×10^{-14}				○
142	I001Z1M10R5			10	10^{-5}	3.11	3.78×10^{-16}				×
143	I001Z1M10R3			10	10^{-3}	3.11	3.78×10^{-15}				○
144	I001Z1M10R1			10	10^{-1}	3.11	3.78×10^{-14}				○

Table 2.3: Same as Table 2.1, but moodel parameters in the case of $C_\zeta = 1$.

	Model	C_ζ	$Z/Z_\odot$	μ_0	β_0	$B_0(\mu\mathrm{G})$	$\Omega_0(\mathrm{s}^{-1})$	$M_{\mathrm{cl}}(M_\odot)$	$T_{\mathrm{cl}}(\mathrm{K})$	$r_{\mathrm{cl}}(\mathrm{au})$	fragmentation
145	I1ZPM3R5			3	10^{-5}	12.1	3.06×10^{-16}				$\times$
146	I1ZPM3R3			3	10^{-3}	12.1	3.06×10^{-15}				$\times$
147	I1ZPM3R1			3	10^{-1}	12.1	3.06×10^{-14}				$\times$
148	I1ZPM5R5			5	10^{-5}	7.27	3.06×10^{-16}				$\times$
149	I1ZPM5R3	1	0	5	10^{-3}	7.27	3.06×10^{-15}	4.79×10^2	24.9	1.74×10^5	$\times$
150	I1ZPM5R1			5	10^{-1}	7.27	3.06×10^{-14}				$\circ$
151	I1ZPM10R5			10	10^{-5}	3.63	3.06×10^{-16}				$\times$
152	I1ZPM10R3			10	10^{-3}	3.63	3.06×10^{-15}				$\times$
153	I1ZPM10R1			10	10^{-1}	3.63	3.06×10^{-14}				$\times$
154	I1Z7M3R5			3	10^{-5}	12.1	3.06×10^{-16}				$\times$
155	I1Z7M3R3			3	10^{-3}	12.1	3.06×10^{-15}				$\times$
156	I1Z7M3R1			3	10^{-1}	12.1	3.06×10^{-14}				$\times$
157	I1Z7M5R5			5	10^{-5}	7.27	3.06×10^{-16}				$\times$
158	I1Z7M5R3	1	10^{-7}	5	10^{-3}	7.27	3.06×10^{-15}	4.79×10^2	24.9	1.74×10^5	$\times$
159	I1Z7M5R1			5	10^{-1}	7.27	3.06×10^{-14}				$\circ$
160	I1Z7M10R5			10	10^{-5}	3.63	3.06×10^{-16}				$\times$
161	I1Z7M10R3			10	10^{-3}	3.63	3.06×10^{-15}				$\times$
162	I1Z7M10R1			10	10^{-1}	3.63	3.06×10^{-14}				$\times$
163	I1Z6M3R5			3	10^{-5}	12.1	3.06×10^{-16}				$\times$
164	I1Z6M3R3			3	10^{-3}	12.1	3.06×10^{-15}				$\times$
165	I1Z6M3R1			3	10^{-1}	12.1	3.06×10^{-14}				$\times$
166	I1Z6M5R5			5	10^{-5}	7.27	3.06×10^{-16}				$\times$
167	I1Z6M5R3	1	10^{-6}	5	10^{-3}	7.27	3.06×10^{-15}	4.79×10^2	24.9	1.74×10^5	$\times$
168	I1Z6M5R1			5	10^{-1}	7.27	3.06×10^{-14}				$\circ$
169	I1Z6M10R5			10	10^{-5}	3.63	3.06×10^{-16}				$\times$
170	I1Z6M10R3			10	10^{-3}	3.63	3.06×10^{-15}				$\times$
171	I1Z6M10R1			10	10^{-1}	3.63	3.06×10^{-14}				$\times$
172	I1Z5M3R5			3	10^{-5}	12.1	3.06×10^{-16}				$\times$
173	I1Z5M3R3			3	10^{-3}	12.1	3.06×10^{-15}				$\times$
174	I1Z5M3R1			3	10^{-1}	12.1	3.06×10^{-14}				$\times$
175	I1Z5M5R5			5	10^{-5}	7.29	3.06×10^{-16}				$\times$
176	I1Z5M5R3	1	10^{-5}	5	10^{-3}	7.29	3.06×10^{-15}	4.82×10^2	25.1	1.74×10^5	$\times$
177	I1Z5M5R1			5	10^{-1}	7.29	3.06×10^{-14}				$\times$
178	I1Z5M10R5			10	10^{-5}	3.64	3.06×10^{-16}				$\times$
179	I1Z5M10R3			10	10^{-3}	3.64	3.06×10^{-15}				$\times$
180	I1Z5M10R1			10	10^{-1}	3.64	3.06×10^{-14}				$\times$
181	I1Z4M3R5			3	10^{-5}	12.4	3.06×10^{-16}				$\times$
182	I1Z4M3R3			3	10^{-3}	12.4	3.06×10^{-15}				$\times$
183	I1Z4M3R1			3	10^{-1}	12.4	3.06×10^{-14}				$\times$
184	I1Z4M5R5			5	10^{-5}	7.42	3.06×10^{-16}				$\times$
185	I1Z4M5R3	1	10^{-4}	5	10^{-3}	7.42	3.06×10^{-15}	5.09×10^2	26.0	1.77×10^5	$\times$
186	I1Z4M5R1			5	10^{-1}	7.42	3.06×10^{-14}				$\circ$
187	I1Z4M10R5			10	10^{-5}	3.71	3.06×10^{-16}				$\times$
188	I1Z4M10R3			10	10^{-3}	3.71	3.06×10^{-15}				$\times$
189	I1Z4M10R1			10	10^{-1}	3.71	3.06×10^{-14}				$\circ$
190	I1Z3M3R5			3	10^{-5}	12.7	3.06×10^{-16}				$\times$
191	I1Z3M3R3			3	10^{-3}	12.7	3.06×10^{-15}				$\times$
192	I1Z3M3R1			3	10^{-1}	12.7	3.06×10^{-14}				$\times$
193	I1Z3M5R5			5	10^{-5}	7.60	3.06×10^{-16}				$\times$
194	I1Z3M5R3	1	10^{-3}	5	10^{-3}	7.60	3.06×10^{-15}	5.43×10^2	27.3	1.81×10^5	$\times$
195	I1Z3M5R1			5	10^{-1}	7.60	3.06×10^{-14}				$\diamond$
196	I1Z3M10R5			10	10^{-5}	3.80	3.06×10^{-16}				$\times$
197	I1Z3M10R3			10	10^{-3}	3.80	3.06×10^{-15}				$\times$
198	I1Z3M10R1			10	10^{-1}	3.80	3.06×10^{-14}				$\circ$
199	I1Z2M3R5			3	10^{-5}	12.1	3.12×10^{-16}				$\times$
200	I1Z2M3R3			3	10^{-3}	12.1	3.12×10^{-15}				$\times$
201	I1Z2M3R1			3	10^{-1}	12.1	3.12×10^{-14}				$\times$
202	I1Z2M5R5			5	10^{-5}	7.28	3.12×10^{-16}				$\times$
203	I1Z2M5R3	1	10^{-2}	5	10^{-3}	7.28	3.12×10^{-15}	4.39×10^2	25.0	1.66×10^5	$\times$
204	I1Z2M5R1			5	10^{-1}	7.28	3.12×10^{-14}				$\circ$
205	I1Z2M10R5			10	10^{-5}	3.64	3.12×10^{-16}				$\times$
206	I1Z2M10R3			10	10^{-3}	3.64	3.12×10^{-15}				$\times$
207	I1Z2M10R1			10	10^{-1}	3.64	3.12×10^{-14}				$\circ$
208	I1Z1M3R5			3	10^{-5}	10.9	3.72×10^{-16}				$\times$
209	I1Z1M3R3			3	10^{-3}	10.9	3.72×10^{-15}				$\times$
210	I1Z1M3R1			3	10^{-1}	10.9	3.72×10^{-14}				$\times$
211	I1Z1M5R5			5	10^{-5}	6.52	3.72×10^{-16}				$\times$
212	I1Z1M5R3	1	10^{-1}	5	10^{-3}	6.52	3.72×10^{-15}	1.58×10^2	20.1	1.06×10^5	$\times$
213	I1Z1M5R1			5	10^{-1}	6.52	3.72×10^{-14}				$\circ$
214	I1Z1M10R5			10	10^{-5}	3.26	3.72×10^{-16}				$\times$
215	I1Z1M10R3			10	10^{-3}	3.26	3.72×10^{-15}				$\circ$
216	I1Z1M10R1			10	10^{-1}	3.26	3.72×10^{-14}				$\circ$

Table 2.4: Same as Table 2.1, but moodel parameters in the case of $C_\zeta = 10$.

	Model	C_ζ	$Z/Z_\odot$	μ_0	β_0	$B_0(\mu\mathrm{G})$	$\Omega_0(\mathrm{s}^{-1})$	$M_{\rm cl}(M_\odot)$	$T_{\rm cl}(\mathrm{K})$	$r_{\rm cl}(\mathrm{au})$	fragmentation
217	I10ZPM3R5			3	10^{-5}	13.5	3.06×10^{-16}				$\times$
218	I10ZPM3R3			3	10^{-3}	13.5	3.06×10^{-15}				$\times$
219	I10ZPM3R1			3	10^{-1}	13.5	3.06×10^{-14}				$\circ$
220	I10ZPM5R5			5	10^{-5}	8.10	3.06×10^{-16}				$\times$
221	I10ZPM5R3	10	0	5	10^{-3}	8.10	3.06×10^{-15}	6.56×10^{2}	31.0	1.93×10^{5}	$\times$
222	I10ZPM5R1			5	10^{-1}	8.10	3.06×10^{-14}				$\times$
223	I10ZPM10R5			10	10^{-5}	4.05	3.06×10^{-16}				$\times$
224	I10ZPM10R3			10	10^{-3}	4.05	3.06×10^{-15}				$\times$
225	I10ZPM10R1			10	10^{-1}	4.05	3.06×10^{-14}				$\circ$
226	I10Z7M3R5			3	10^{-5}	13.5	3.06×10^{-16}				$\times$
227	I10Z7M3R3			3	10^{-3}	13.5	3.06×10^{-15}				$\times$
228	I10Z7M3R1			3	10^{-1}	13.5	3.06×10^{-14}				$\circ$
229	I10Z7M5R5			5	10^{-5}	8.10	3.06×10^{-16}				$\times$
230	I10Z7M5R3	10	10^{-7}	5	10^{-3}	8.10	3.06×10^{-15}	6.57×10^{2}	31.0	1.93×10^{5}	$\times$
231	I10Z7M5R1			5	10^{-1}	8.10	3.06×10^{-14}				$\times$
232	I10Z7M10R5			10	10^{-5}	4.05	3.06×10^{-16}				$\times$
233	I10Z7M10R3			10	10^{-3}	4.05	3.06×10^{-15}				$\times$
234	I10Z7M10R1			10	10^{-1}	4.05	3.06×10^{-14}				$\circ$
235	I10Z6M3R5			3	10^{-5}	13.5	3.06×10^{-16}				$\times$
236	I10Z6M3R3			3	10^{-3}	13.5	3.06×10^{-15}				$\times$
237	I10Z6M3R1			3	10^{-1}	13.5	3.06×10^{-14}				$\times$
238	I10Z6M5R5			5	10^{-5}	8.10	3.06×10^{-16}				$\times$
239	I10Z6M5R3	10	10^{-6}	5	10^{-3}	8.10	3.06×10^{-15}	6.57×10^{2}	31.0	1.93×10^{5}	$\times$
240	I10Z6M5R1			5	10^{-1}	8.10	3.06×10^{-14}				$\times$
241	I10Z6M10R5			10	10^{-5}	4.05	3.06×10^{-16}				$\times$
242	I10Z6M10R3			10	10^{-3}	4.05	3.06×10^{-15}				$\times$
243	I10Z6M10R1			10	10^{-1}	4.05	3.06×10^{-14}				$\circ$
244	I10Z5M3R5			3	10^{-5}	13.6	3.06×10^{-16}				$\times$
245	I10Z5M3R3			3	10^{-3}	13.6	3.06×10^{-15}				$\times$
246	I10Z5M3R1			3	10^{-1}	13.6	3.06×10^{-14}				$\times$
247	I10Z5M5R5			5	10^{-5}	8.13	3.06×10^{-16}				$\times$
248	I10Z5M5R3	10	10^{-5}	5	10^{-3}	8.13	3.06×10^{-15}	6.64×10^{2}	31.2	1.94×10^{5}	$\times$
249	I10Z5M5R1			5	10^{-1}	8.13	3.06×10^{-14}				$\times$
250	I10Z5M10R5			10	10^{-5}	4.07	3.06×10^{-16}				$\times$
251	I10Z5M10R3			10	10^{-3}	4.07	3.06×10^{-15}				$\times$
252	I10Z5M10R1			10	10^{-1}	4.07	3.06×10^{-14}				$\circ$
253	I10Z4M3R5			3	10^{-5}	14.0	3.06×10^{-16}				$\times$
254	I10Z4M3R3			3	10^{-3}	14.0	3.06×10^{-15}				$\times$
255	I10Z4M3R1			3	10^{-1}	14.0	3.06×10^{-14}				$\times$
256	I10Z4M5R5			5	10^{-5}	8.38	3.06×10^{-16}				$\times$
257	I10Z4M5R3	10	10^{-4}	5	10^{-3}	8.38	3.06×10^{-15}	7.25×10^{2}	33.1	1.99×10^{5}	$\times$
258	I10Z4M5R1			5	10^{-1}	8.38	3.06×10^{-14}				$\circ$
259	I10Z4M10R5			10	10^{-5}	4.19	3.06×10^{-16}				$\times$
260	I10Z4M10R3			10	10^{-3}	4.19	3.06×10^{-15}				$\times$
261	I10Z4M10R1			10	10^{-1}	4.19	3.06×10^{-14}				$\circ$
262	I10Z3M3R5			3	10^{-5}	15.3	3.07×10^{-16}				$\times$
263	I10Z3M3R3			3	10^{-3}	15.3	3.07×10^{-15}				$\times$
264	I10Z3M3R1			3	10^{-1}	15.3	3.07×10^{-14}				$\times$
265	I10Z3M5R5			5	10^{-5}	9.16	3.07×10^{-16}				$\times$
266	I10Z3M5R3	10	10^{-3}	5	10^{-3}	9.16	3.07×10^{-15}	9.39×10^{2}	39.6	2.17×10^{5}	$\times$
267	I10Z3M5R1			5	10^{-1}	9.16	3.07×10^{-14}				$\diamond$
268	I10Z3M10R5			10	10^{-5}	4.58	3.07×10^{-16}				$\times$
269	I10Z3M10R3			10	10^{-3}	4.58	3.07×10^{-15}				$\times$
270	I10Z3M10R1			10	10^{-1}	4.58	3.07×10^{-14}				$\diamond$
271	I10Z2M3R5			3	10^{-5}	15.3	3.13×10^{-16}				$\times$
272	I10Z2M3R3			3	10^{-3}	15.3	3.13×10^{-15}				$\times$
273	I10Z2M3R1			3	10^{-1}	15.3	3.13×10^{-14}				$\diamond$
274	I10Z2M5R5			5	10^{-5}	9.16	3.13×10^{-16}				$\times$
275	I10Z2M5R3	10	10^{-2}	5	10^{-3}	9.16	3.13×10^{-15}	8.67×10^{2}	39.6	2.09×10^{5}	$\times$
276	I10Z2M5R1			5	10^{-1}	9.16	3.13×10^{-14}				$\circ$
277	I10Z2M10R5			10	10^{-5}	4.58	3.13×10^{-16}				$\times$
278	I10Z2M10R3			10	10^{-3}	4.58	3.13×10^{-15}				$\times$
279	I10Z2M10R1			10	10^{-1}	4.58	3.13×10^{-14}				$\circ$
280	I10Z1M3R5			3	10^{-5}	12.6	3.61×10^{-16}				$\times$
281	I10Z1M3R3			3	10^{-3}	12.6	3.61×10^{-15}				$\times$
282	I10Z1M3R1			3	10^{-1}	12.6	3.61×10^{-14}				$\circ$
283	I10Z1M5R5			5	10^{-5}	7.54	3.61×10^{-16}				$\times$
284	I10Z1M5R3	10	10^{-1}	5	10^{-3}	7.54	3.61×10^{-15}	2.74×10^{2}	26.8	1.29×10^{5}	$\times$
285	I10Z1M5R1			5	10^{-1}	7.54	3.61×10^{-14}				$\circ$
286	I10Z1M10R5			10	10^{-5}	3.77	3.61×10^{-16}				$\times$
287	I10Z1M10R3			10	10^{-3}	3.77	3.61×10^{-15}				$\times$
288	I10Z1M10R1			10	10^{-1}	3.77	3.61×10^{-14}				$\circ$

Chapter 3

Results & Discussion

3.1 Fragmentation conditions

3.1.1 Environmental dependency

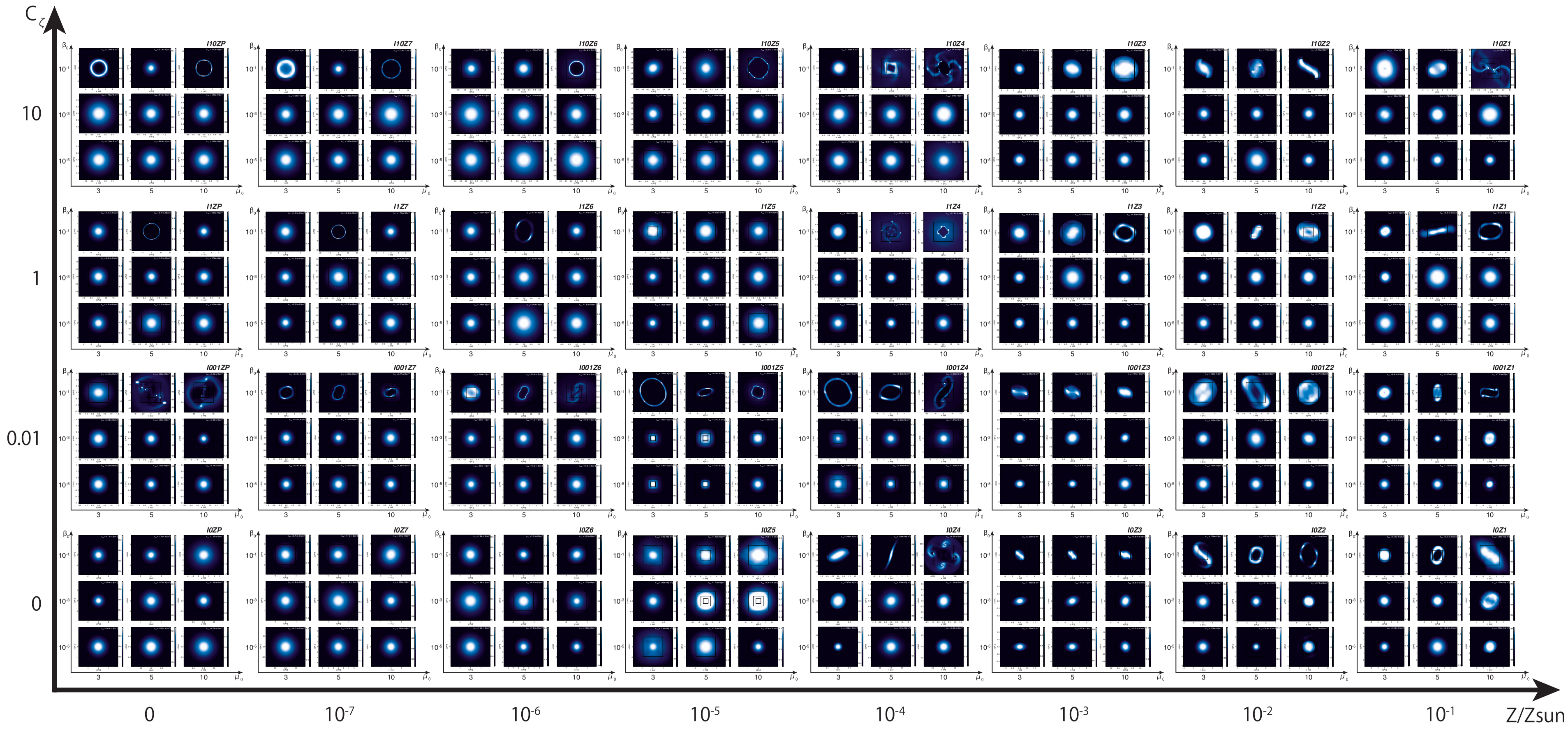

Figure 3.1: 288 panels are the calculation results for each model. The density distribution in the $z = 0$ plane is plotted. One set with nine panels, and plots of these distribution of each model with models arranged based on the ratio of rotational energy to gravitational energy β_0 (vertical axis) and the mass-to-flux ratio μ_0 (horizontal axis). Further, a set of nine group is arranged on the horizontal axis the ionization strengths (C_ζ) and the vertical axis metallicities ($Z/\,Z_\odot$).

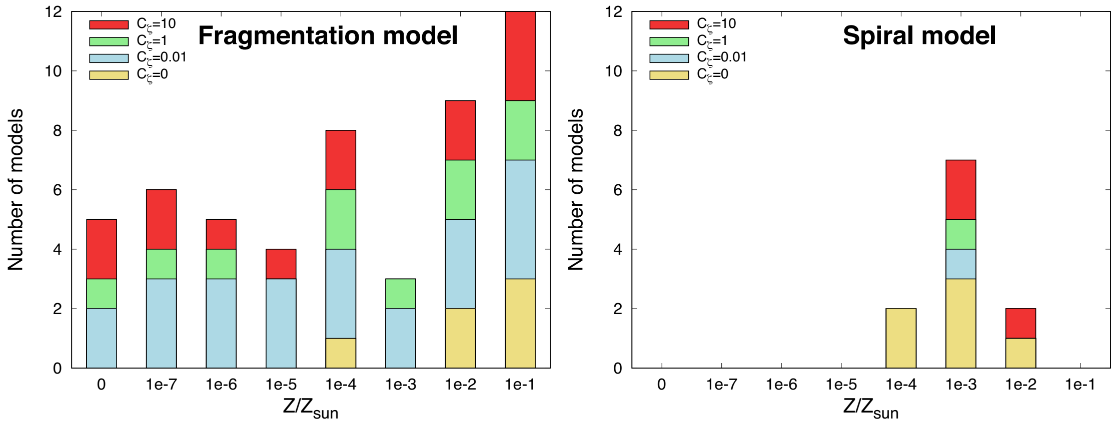

Figure 3.2: The histogram of model with fragmentation (left panel) and model with spiral (right panel).

The calculation results of 288 cases are shown in Fig.3.1. Each panel represents the density distribution in the $z = 0$ plane. For the cases where fragmentation occurs, snapshots at that stage are plotted, whereas for the cases not resulting in fragmentation, snapshots at the central number density $n_c \sim 10^{16}\,\mathrm{cm}^{-3}$ are plotted. The nine panels of 3×3 are one set, and the horizontal axis of these 9 panels is the mass-to-flux ratio μ_0, and the vertical axis is the ratio of rotational energy to gravitational energy β_0. 32 sets of them (3×3) are arranged on the horizontal axis the ionization strengths (C_ζ) and the vertical axis metallicities ($Z/\,Z_\odot$), for example, the lower left panel is the model I0ZP ($C_\zeta = 0$, $Z/\,Z_\odot = 0$) and corresponds to a primordial environment. I simply summarized the outcomes in Fig.3.2, in which the vertical axis is the number of model and horizontal axis is the metallicity. In Fig.3.2, the left panel is the number of models in which fragmentation occurs and the right panel is the number of models in which a spiral structure develops without occurring fragmentation.

There is a difference in the fragmentation process depending on the combination of the ionization parameter C_ζ and the metallicity $Z/\,Z_\odot$ in collapsing cloud environment (Fig.3.1). As metallicity increases, the number of cases of fragmentation increases (Fig.3.2). In the case of a primordial environment with no ionization sources ($C_\zeta = 0$) in particular, the tendency is remarkable. In general, gas cooling promotes cloud deformation to filaments, but the heating process stabilizes the gas against aspherical perturbations (Lai 2000, Hanawa and Matsumoto 2000, Chiaki et al. 2016). In the case of $C_\zeta = 0$ and $Z/Z_\odot \leq 10^{-5}$, there is no dust with high cooling efficiency, so the effective ratio of specific heat γ is almost 1, and the contraction proceeds isothermally until a protostar is formed (Susa et al. 2015, Higuchi et al. 2018). Therefore, in the model I0ZP, I0Z7, I0Z6, and I0Z5, there is no fragment during collapsing phase. Gas cooling becomes effective clearly in higher metallicity cases, and gas cooling makes the cloud flat. As a result, in models with a metallicity ($Z/Z_\odot > 10^{-5}$), there are many fragment.

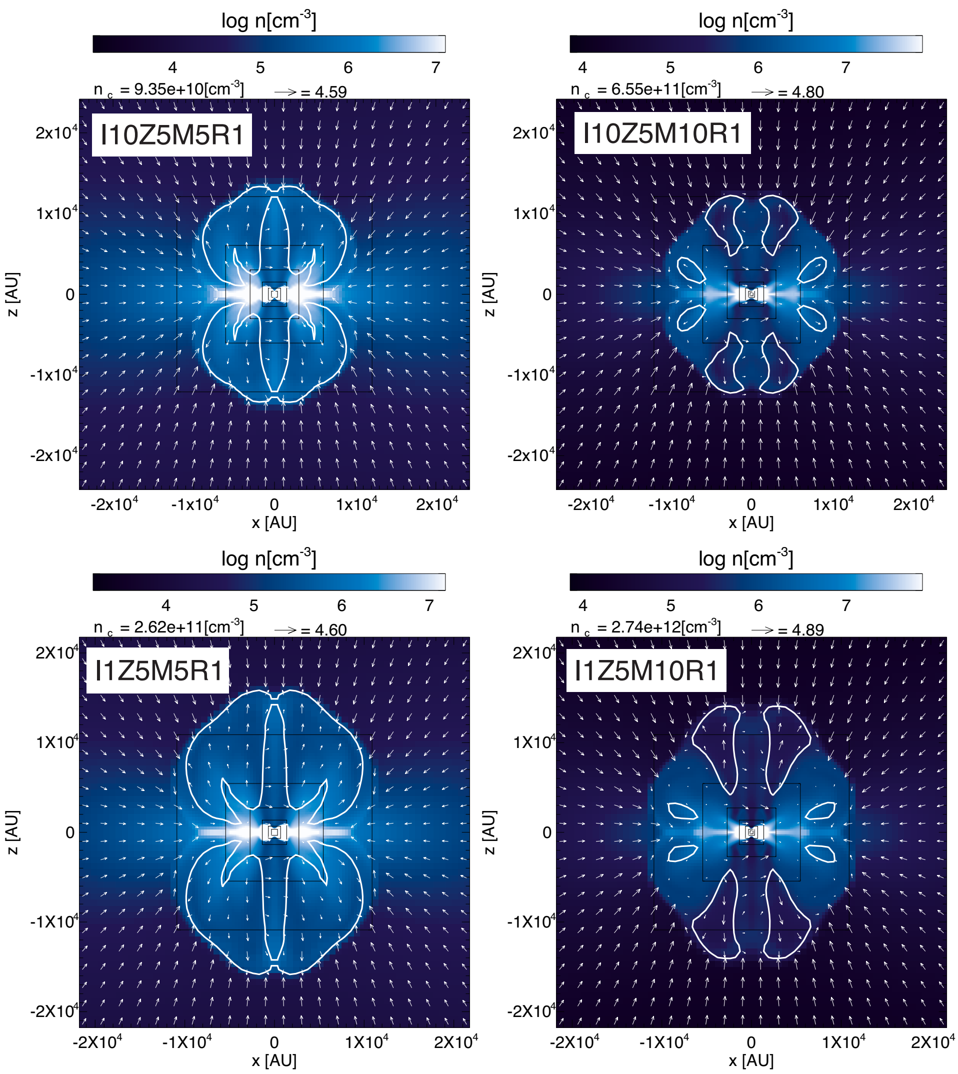

Figure 3.3: Low-density outflows. Density (color) and velocity (arrows) distributions in the $y = 0$ plane for model I10Z5M5R1 (top left), I10Z5M10R1 (top right), I1Z5M5R1 (bottom left), and I1Z5M10R1 (bottom right). The central density n_c is given above each panel.

When compared with the same metallicity, there is a tendency for fragments to occur in models with high ionization strength. This is because, in the case of $C_\zeta = 0.01, 1,$ and 10 and $Z/Z_\odot \leq 10^{-5}$, the ionization strength is high, and HD with high cooling efficiency is formed (Galli and Palla 1998, Nakamura and Umemura 2002). The difference between $C_\zeta = 0.01, 1$ and 10 is whether or not the low-density outflow is driven (Fig. 3.3) (for detail, see Higuchi et al. 2019). The outflow sweeps a large fraction of infalling gas with large angular momentum, therefore, the models of $C_\zeta = 0.01$, where the outflow does not appear, are easier to fragment than others. In addition, it can be considered that the high resistivity is also caused by fragmentation. The magnetic field can suppress the fragmentation of the collapsing core by transmitting angular momentum through the magnetic braking and outflow (e.g., Machida et al. 2007, 2008a, Price and Bate 2007). Higuchi et al. (2018) indicates that the smaller the ionization parameter, the higher the resistivity. In the models of $C_\zeta = 0.01$, it is thought that fragmentation is promoted by the dissipation of the magnetic field. In the range of $10^{-4} \leq Z/Z_\odot \leq 10^{-2}$, many models show the spiral structure but do not show fragmentation. Such a structure is reported also by Chiaki et al. (2016). Summarizing the results, out of 288 models, 51 models show fragmentation, 11 models are not, but a spiral structure are formed.

3.1.2 The effect of the initial magnetic filed and rotation

Next, we look at each of the nine panels (3×3 diagrams of β_0–μ_0 plane). In general, a model with higher β_0 and μ_0 shows fragmentation. In the primordial environment, such as the forming site of first star, the contribution of the magnetic field (μ_0) and rotation (β_0) to the fragmentation has also been investigated in Machida et al. (2004, 2005, 2008a). A similar trend can be seen in that study. In the present parameter survey, it is found that fragmentation can occur in the parameter range of $\beta_0 > 10^{-3}$. As for μ_0, fragment occurs when it is higher than about 3. This tendency is remarkable in $Z/Z_\odot \geq 10^{-4}$. In the case of $Z/Z_\odot \leq 10^{-6}$, however, fragmentation appears in both $\mu_0 = 3$ and 5, but fragmentation does not appear in $\mu_0 = 10$ (such as model I10ZP, I10Z7, I1ZP, and I1Z7). The strong magnetic field slows the collapse, so the oblateness tends to increase, and the fragmentation can be promoted. Moreover, the degree of magnetic field dissipation differs depending on the environments, so that the initial mass-to-flux ratio may make a difference at the stage of fragmentation. This result is limited to the collapsing phase, so a long time simulation is required.

3.2 Timing of fragmentation

In Sec.3.1.2, we discussed the fragmentation conditions from the viewpoint of the initial conditions, while in this section, we discuss the timing of fragmentation. Fig.3.4 shows (A) Mass-to-Flux ratio μ, (B) central angular velocity Ω_c, and (c) the ratio of rotational energy to gravitational energy β for the model I1Z1. The oblateness of the cloud (horizontal axis in Fig.3.4) is calculated as

$$\epsilon_{\rm ob} \equiv \sqrt{h_{\rm l} h_{\rm s}}/h_{\rm z} \tag{3.1}$$

where $h_{\rm l}$, $h_{\rm s}$, and $h_{\rm z}$ are the length of the long-, short- and z-axis for the gas with $\rho > 0.01\rho_{\rm max}$, respectively (for detail of the determination of each length, see Matsumoto and Hanawa 1999, Machida et al. 2004). The different models are represented by different line colors and/or symbols, for example, model I1Z1M10R1 ($C_\zeta = 1$ and $Z/\,Z_\odot = 10^{-1}$, $\mu_0 = 10$, and $\beta_0 = 10^{-1}$) has a solid red line with a triangle symbol. In Fig.3.4 (C), the color of lines (gray to black) indicates the ratio of $\rho_{\rm max}(r \neq 0)$ to ρ_c in log scale, that is, the black shows that the fragmentation has occurred in the model.

3.2.1 Collapse geometry

Before discussing all nine models in Fig.3.4, we discuss a closer look with one model (model I1Z1M10R1) in Fig.3.5. Fig.3.5 (A) shows only model I1Z1M10R1 extracted from central angular velocity Ω_c. Fig.3.5 (B) shows the time evolution of disk radius. The color indicates the maximum number density, that is, it represents time evolution of cloud. Fig.3.5 shows that, during the early stage of evolution, the cloud collapses maintaining nearly spherical symmetry (i to ii). Then, the cloud contracts flatly due to the magnetic tension force in the isothermal phase (ii to iii, $n_{\rm max} \leq 10^{11}\,{\rm cm}^{-3}$). The oblateness of cloud is high ($\epsilon_{\rm ob} > 10$), but μ and β are low, therefore, no fragment has occurred (see other than the line with the triangle symbol in Fig.3.4 (A) and (C)). In the adiabatic phase (see fig.2 in Higuchi et al. 2018), the gas pressure works isotropically, and the oblateness becomes low (iii to iv, $n_{\rm max} > 10^{11}\,{\rm cm}^{-3}$). The first core is formed at $n_{\rm max} \sim 10^{11}\,{\rm cm}^{-3}$. This core is in a quasi-hydrostatic state after its formation, thus, it slowly contracts. Then, since the gas with a large angular momentum accretes from the envelope to the first core, $\epsilon_{\rm ob}$ becomes high again and β becomes high and fragment appears (iv to v, see also Fig.3.4 (c)). In the case of model I1Z1, in the range $10^{11} < \frac{n_{\rm max}}{\rm cm^{-3}} < 10^{16}$, the magnetic field can be dissipated by Ohmic dissipation (see fig.9 (h) in Higuchi et al. 2018). The rapid rise of μ is due to the dissipation of the magnetic field, and the fragmentation is promoted due to the weakening of the magnetic field strength (see model I1Z1M10R1 (red line) in Fig.3.4 (A)).

Fig.3.6 shows (A) the central angular velocity Ω_c and (b) the disk radius for the model I1Z1M3R1. The fragmentation does not occur in this model. The difference from model I1Z1M10R1 is the initial mass-to-flux ratio. From i to v, like model I1Z1M10R1, it evolves with repeating increase and decrease of oblateness. Since the initial magnetic field strength is strong, fragmentation is suppressed, and the evolution progresses without fragmentation (see also model I1Z1M3R1 in Fig.3.4 (A) and (C)). As a result, for the model I1Z1, it is considered that $\epsilon_{\rm ob} \geq 5$, $\mu \geq 0.6 - 1.0$, and $\beta \geq 10^{-2}$ are necessary for fragmentation to occur.

3.2.2 Comparison among models with different parameters of metallicity

Figs.3.7–3.13 show (A) Mass-to-Flux ratio μ, (B) central angular velocity Ω_c, and (c) the ratio of rotational energy to gravitational energy β like Fig.3.4, but simulation results with different models. In all model, during the collapsing phase of the star formation process, it is necessary for fragmentation that the magnetic field is low (μ becomes higher), the cloud shape becomes flat ($\epsilon_{\rm ob}$ become higher), and the rotation is fast (β becomes higher). Figs.3.4–3.13 employ the same value of the ionization parameter $C_\zeta = 1$ and show the difference in metallicity. Considering the model I1Z1 to I1ZP, for the fragmentation, $\epsilon_{\rm ob} \geq 5$, $\mu \geq 0.6 - 1.0$, and $\beta \geq 10^{-2}$ in present work.

In Figs.3.1 and 3.10, fragmentation does not occur in the model I1Z5 (see Fig.3.3

for low-density outflow of model I1Z5M5R1 and I1Z5M10R1). I suggest driving low-density outflow (Higuchi et al. 2019) as one of the reasons. Outflow can transport gas with angular momentum to the outside, so it is likely that the success of extracting angular momentum outwardly led to suppression of fragmentation. However, since this flow also occurs in other models, such as model I1ZP (see also Higuchi et al. 2019), suppression of fragmentation cannot be explained by the flow only. I consider that a more important factor is the dissipation of the magnetic field. In the model of $Z/Z_{\odot} \leq 10^{-6}$, since the magnetic Reynolds number is always 1 or more, magnetic field is dissipated (for detail see Higuchi et al. 2018). In the model of $Z/Z_{\odot} = 10^{-5}$, the magnetic dissipation occurs as the amount of dust increases in the range of $10^{15} \leq \frac{n_c}{\mathrm{cm^{-3}}} \leq 10^{17}$. It is possible that the magnetic field weakens and the contraction progresses, avoiding fragmentation.

Higuchi et al. (2018) shows that the magnetic field does not dissipate during collapsing phase for model I1ZP, I1Z7, and I1Z6. This is because the contraction timescale is shorter than the magnetic field dissipating timescale (for details, see fig.9 in Higuchi et al. 2018). Thus, magnetic field does not dissipate and mass-to-Flux ratio does not become high in the model I1ZP, I1Z7, and I1Z6 (Fig.3.11 (A), 3.12 (A), and 3.13 (A)) Isothermal collapse continues without forming adiabatic core until protostar formation. Therefore, fragmentation is unlikely to occur in the collapsing phase. This is particularly noticeable in the case of $C_{\zeta} = 0$, such as model I0ZP, I0Z7, and I0Z6. In the model I1ZP, I1Z7, and I1Z6, however, after the gas density of the collapsing cloud becomes $n_c \sim 10^9\,\mathrm{cm^{-3}}$, the gas temperature rapidly rises by the three-body reaction of hydrogen atoms (e.g., Palla et al. 1983, Omukai et al. 2005), and the gas pressure increase (Omukai et al. 2005, Higuchi et al. 2018). Therefore, the collapse slows down, and during which a parcel of gas with a large angular momentum can accrete from the outer region. As a result, ϵ_{ob} becomes high and fragmentation occurs in the model I1Z6M5R1 (Fig.3.11), I1Z7M5R1 (Fig.3.12), and I1ZPM5R1 (Fig.3.13).

3.2.3 Comparison among models with different parameters of ionization strength

Figs.3.14–3.16 unify models with metallicity $Z/Z_\odot = 0$ and show the difference in the ionization strength. Figs.3.14–3.16 show (A) Mass-to-Flux ratio μ, (B) central angular velocity Ω_c, and (c) the ratio of rotational energy to gravitational energy β like Fig.3.4, but with different models. Similar to the result of comparison of different values of metallicity, if the conditions of $\epsilon_{\rm ob} \geq 5$, $\mu \geq 0.6 - 1.0$, and $\beta \geq 10^{-2}$ are satisfied, the possibility of fragmentation is high.

I find that the fragmentation occurs more frequently in model I001ZP and I10ZP rather than model I0ZP. This is due to the adiabatic core formation and the magnetic dissipation. Fig.3.14 shows the result of model I0ZP, in which there are neither ionization sources nor metals supplied by past supernovae. There is no dust, and electrons carry the charge. Therefore, the resistivity is low and the magnetic field is not dissipated (for detail see Higuchi et al. 2018). Fragmentation is promoted by the dissipation of the magnetic field. In this respect, in the model I0ZP, since the magnetic field continues to be amplified, fragmentation is unlikely to occur. However, we should consider another factor that the formation of the adiabatic core and the slow contraction cause the accretion of gas with large angular momentum, which is another factor that promotes fragmentation. Because the adiabatic core is not formed in this model, it is possible that fragmentation does not occur in the collapsing phase. However, as the protostar begins to form, the collapse slows. Thus, there is a high probability of fragmentation at that time. In fact, Fig.3.14 (C) indicates that the external density is getting higher than the central density just before the end of the simulation in model I0ZPM5R1. Similarly, model I0ZPM10R1 has a high β and the cloud's oblateness is also sufficiently high. Thus, it is expected that there is a high possibility of fragmentation after the termination of the numerical integrations.

The result of model I001ZP is shown in Fig.3.15. The presence of ionization sources increases the amount of electrons and causes the formation of HD, which enhances radiative cooling, so that the temperature in model I001ZP is lower than in model I0ZP in the range of $n_c \leq 10^8\,{\rm cm}^{-3}$. After that, the temperature rapidly rises due to the three-body reaction of hydrogen atoms, and adiabatic core is temporarily formed (Higuchi et al. 2018, 2019). The same applies to the model I10ZP, which is different from model I0ZP. As described above, even with model I001ZP, fragmentation is confirmed in models that satisfied the fragmentation conditions. The model I001ZPM3R1 also realized this condition near the end of the simulation, and is expected to fragment in the future.

3.3 Additional parameter experiments

In Sec.3.1.2, the fragmentation condition and its timing were discussed using the calculation results of 288 models. Summarizing the results, I find that fragmentation occurs in the parameter range of $\beta_0 > 10^{-3}$ and $\mu_0 > 3$. Additionally, I suggest that if the conditions of $\epsilon_{\rm ob} \geq 5$, $\mu \geq 0.6 - 1.0$, and $\beta \geq 10^{-2}$ are satisfied, the possibility of fragment is high. In the following sections, I show additional calculations limited to specific models, in order to more closely examine the detailed fragmentation conditions based on these results.

3.3.1 Model I1ZP

In Sec.3.3.1, I summarize the results of additional calculations for model I1ZP. As seen in Fig.3.1, each panel shows a density distribution in the $z = 0$ plane. The horizontal axis is the mass-to-flux ratio μ_0, and the vertical axis is the ratio of rotational energy to gravitational energy β_0. For μ_0, I calculated the additional case of $\mu_0 = 30$. For β_0, I performed the calculations in the range of $1.0 \times 10^{-2} \leq \beta_0 \leq 1.0 \times 10^{-1}$ in increments of about 0.02. Fig.3.18 shows the mass-to-flux ratio of (A) $\mu_0 = 3$, (B) $\mu_0 = 5$, (C) $\mu_0 = 10$, and (D) $\mu_0 = 30$ for model I1ZP. On the other hands, Fig.3.19 shows the ratio of rotational energy to gravitational energy of (A) $\mu_0 = 3$, (B) $\mu_0 = 5$, (C) $\mu_0 = 10$, and (D) $\mu_0 = 30$ for the model I1ZP. It was found that for the model I1ZP, the initial fragmentation conditions are roughly described as $\mu_0 \geq 10$ and $\beta_0 \geq 3.0 \times 10^{-2}$. However, in the models around the upper right part of Fig.3.17, μ_0 and β_0 are high, but no fragmentation occurs. Figs.3.18 and 3.19 indicate that models I1ZPM10R1, I1ZPM10R007, and I1ZPM10R1 satisfy the conditions of $\epsilon_{\rm ob} \geq 5$, $\mu \geq 0.6 - 1.0$, and $\beta \geq 10^{-2}$, but fragment does not appear during the collapsing phase. These models are likely to fragment in a further stage and will show a closed binary system. If these binaries gain a lot of mass and grows into a massive star binary, it can be the origin of the black hole binary.

3.3.2 Model I1Z4

In Sec.3.3.2, we summarize the results of additional calculations for model I1Z4. Figs.3.20, 3.21, and 3.22 show the calculation results for the model I1Z4. Each figure is similar to the figure in Sec.3.3.1. Like the model I1ZP, models with higher μ_0 and β_0 tend to show fragmentation. In addition, for the model I1Z4M30R1, bar-mode fragmentation can be confirmed rather than the ring-mode fragmentation seen elsewhere. These fragmentation modes are discussed in Machida et al. (2008b). The initial core with nonaxisymmetric perturbation causes a bar-mode fragmentation. Since the non-axisymmetric perturbation is the same among models, it is considered that the perturbation has grown sufficiently during the collapse for the model I1Z4M30R1. It is confirmed that the long/short axis ratio significantly increases.

3.3.3 Model I001ZP

In Sec.3.3.3, I summarize the results of additional calculations for model I001ZP. Figs.3.23, 3.24, and 3.25 show the calculation results for model I001ZP. Each figure is similar to the figure in Sec.3.3.1. In the model of $\mu_0 = 3$, no matter what value was given to β_0 in the initial condition, it did not fragment. In the range of $\mu_0 > 3$, the fragment appears in models with β_0 of 3.0×10^{-2} or high. However, for model I001ZPM3R1, in terms of fragmentation conditions, it is not strange to occur fragmentation in the future (Figs.3.24, and 3.25).

3.3.4 Model I001Z7

In Sec.3.3.4, I summarize the results of additional calculations for model I001Z7. Figs.3.26, 3.27, and 3.28 show the calculation results for model I001Z7. Each figure is similar to the figure in Sec.3.3.3. Compared with model I001ZP, fragmentation occurs in model I001Z7M3R1, and when the metallicity is high, fragmentation tends to occur even if the initial magnetic field is strong (Figs.3.27 and 3.28).

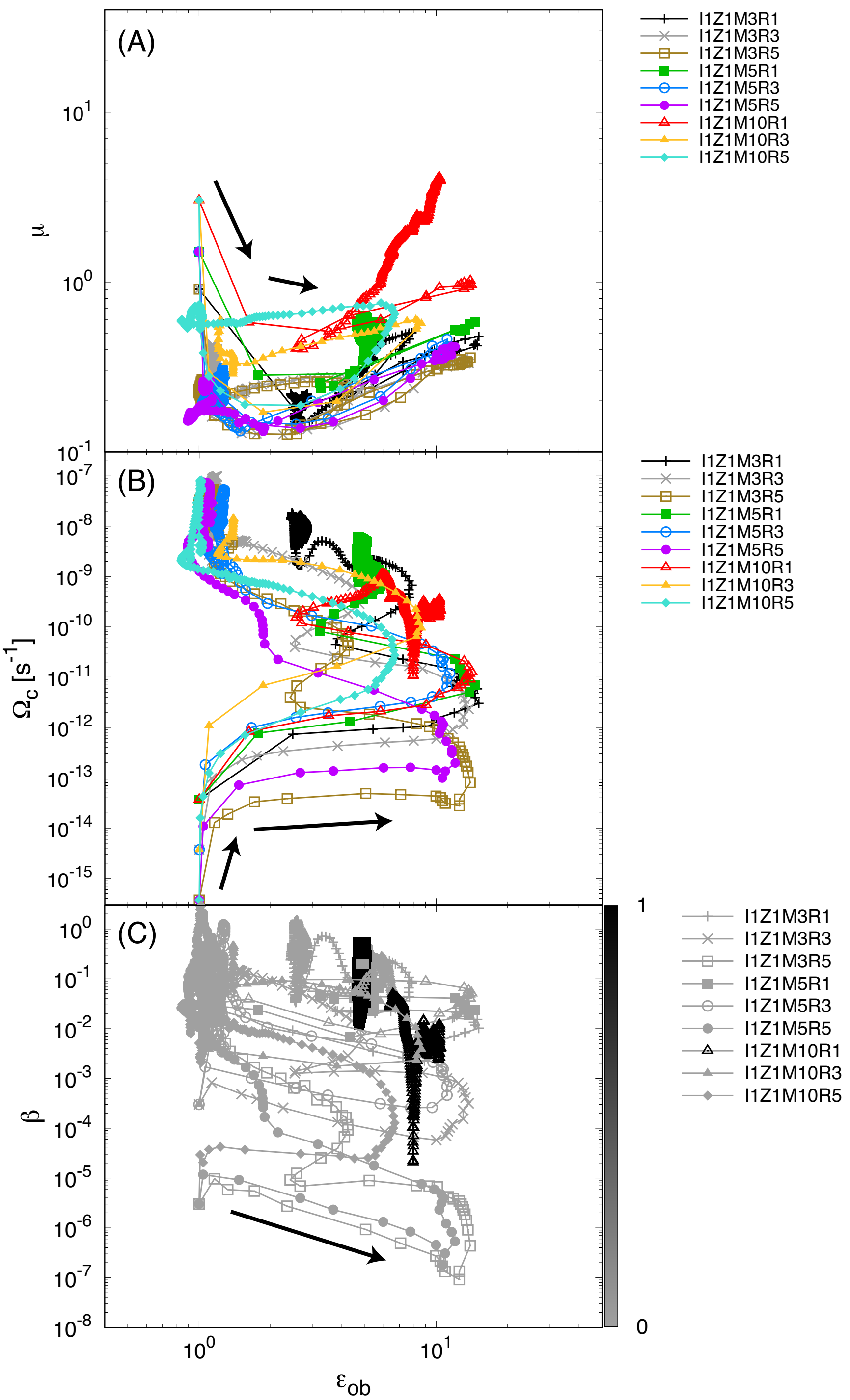

Figure 3.4: The results of model I1Z1 ($C_\zeta = 1$ and $Z/Z_\odot = 10^{-1}$). Top panel is the value of mass-to-flux ratio in the region $\rho > 0.01\rho_{\rm max}$. Middle panel is central angular velocity. Bottom panel is the ratio of rotational energy to gravitational energy and the color contour (gray to black) represents $\rho_{\rm max}/\rho_{\rm c}$. Displayed in black when the $\rho_{\rm max}$ value is 10 or more times the central density value. The horizontal axis is the oblateness of collapsing cloud. Approximate evolution path guidelines from initial conditions are indicated by black arrows.

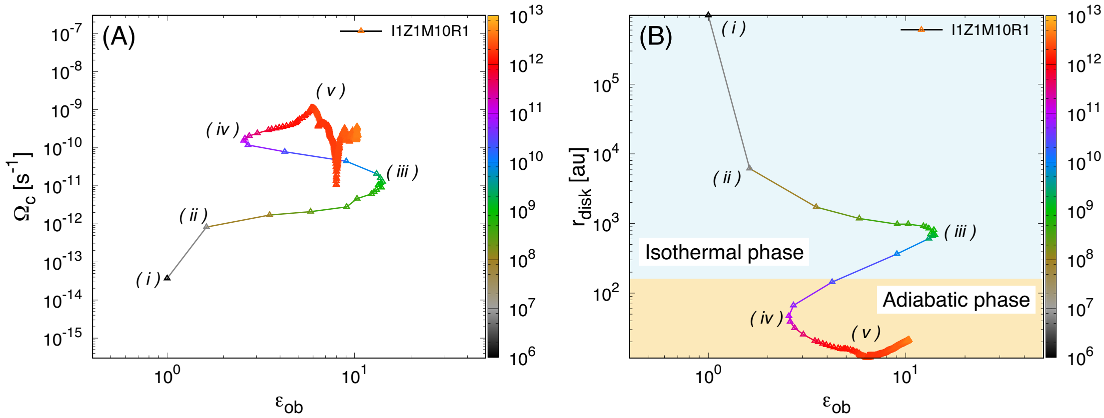

Figure 3.5: (A) the central angular velocity and (B) the disk radius with respect to the oblateness of collapsing cloud for model I1Z1M10R1 ($C_\zeta = 1$, $Z/\,Z_\odot = 0$, $\mu_0 = 10$, and $\beta_0 = 10^{-1}$). The color represents maximum number density $n_{\rm max}\,{\rm cm}^{-3}$.

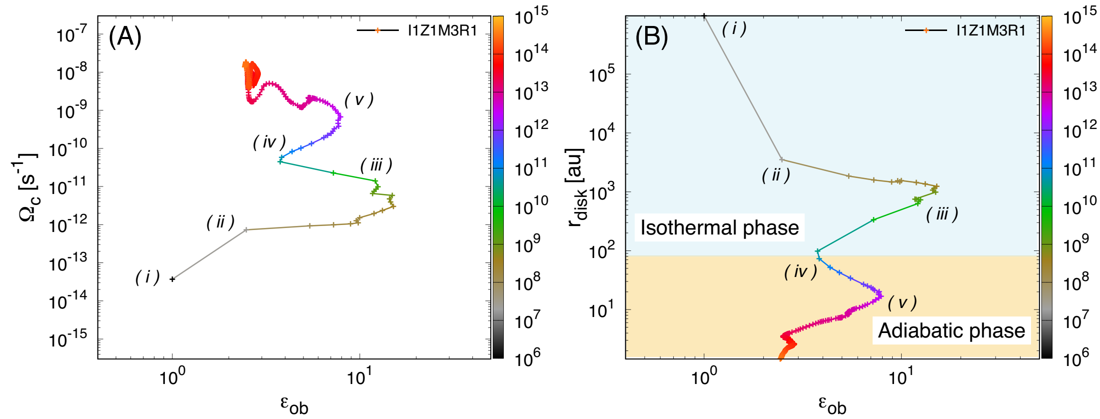

Figure 3.6: Same as Fig.3.5, but for model I1Z1M3R1 ($C_\zeta = 1$ and $Z/\,Z_\odot = 10^{-1}$, $\mu_0 = 3$, and $\beta_0 = 10^{-1}$).

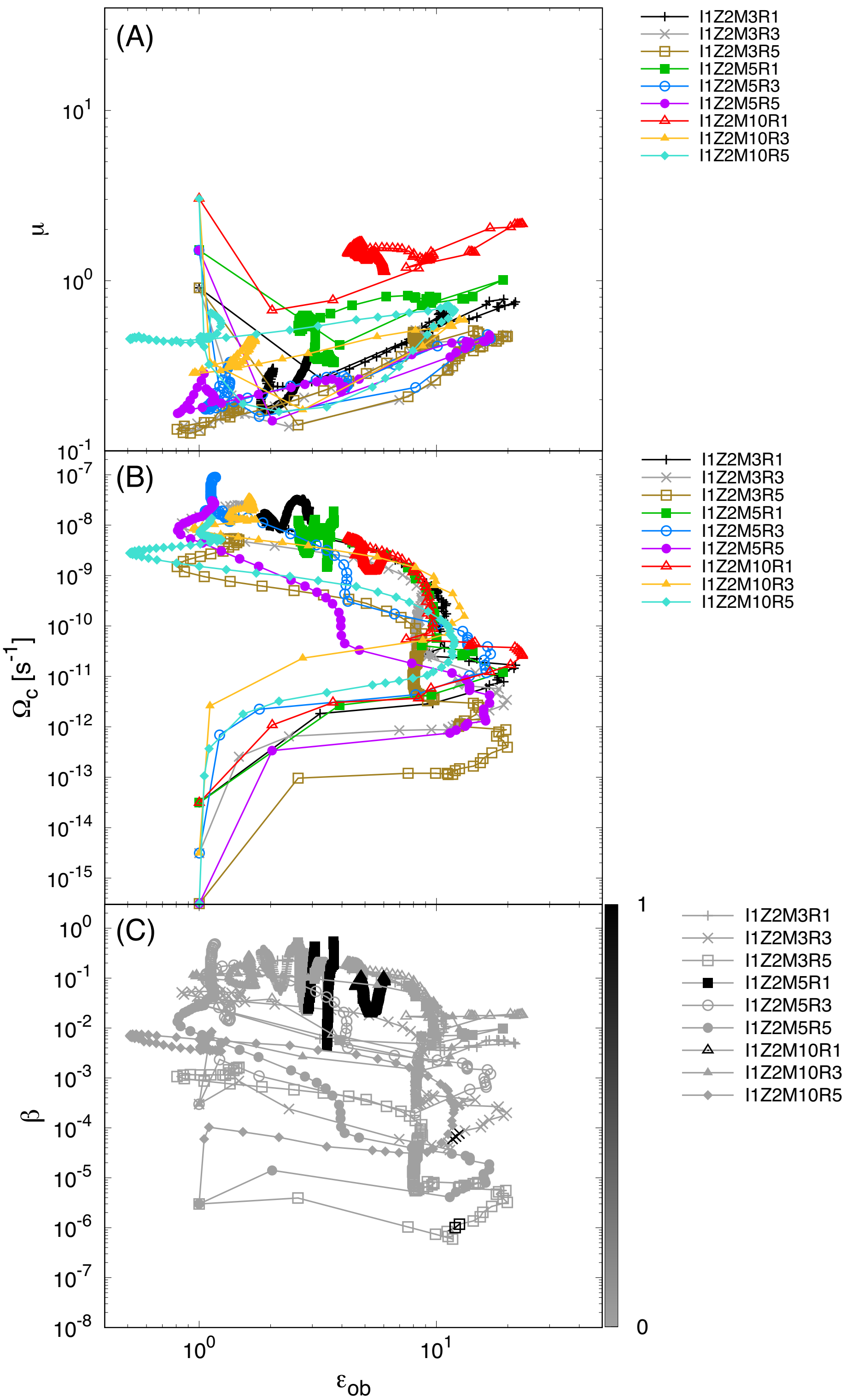

Figure 3.7: Same as Fig.3.4, but for model I1Z2 ($C_\zeta = 1$ and $Z/Z_\odot = 10^{-2}$)

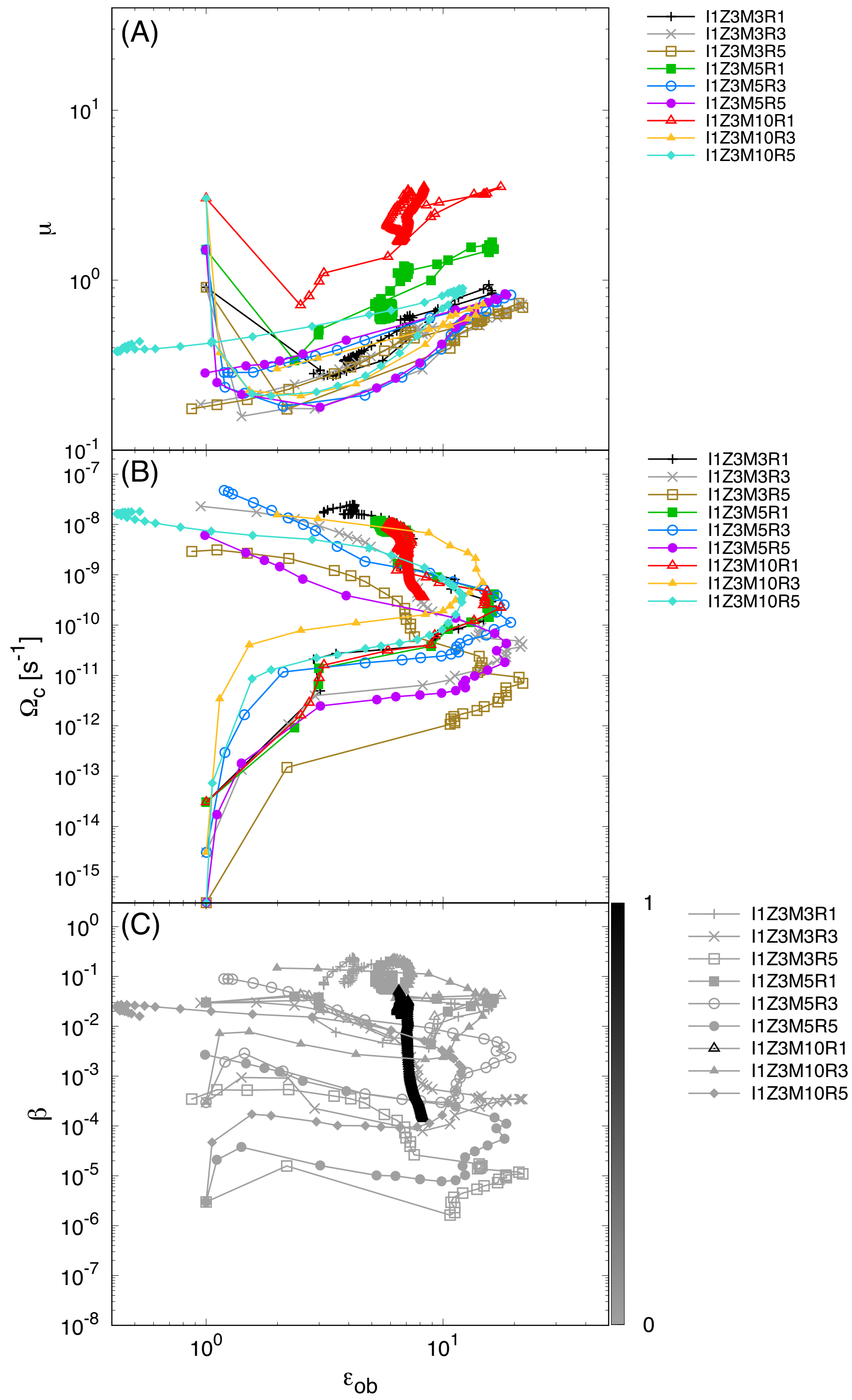

Figure 3.8: Same as Fig.3.4, but for model I1Z3 ($C_\zeta = 1$ and $Z/Z_\odot = 10^{-3}$)

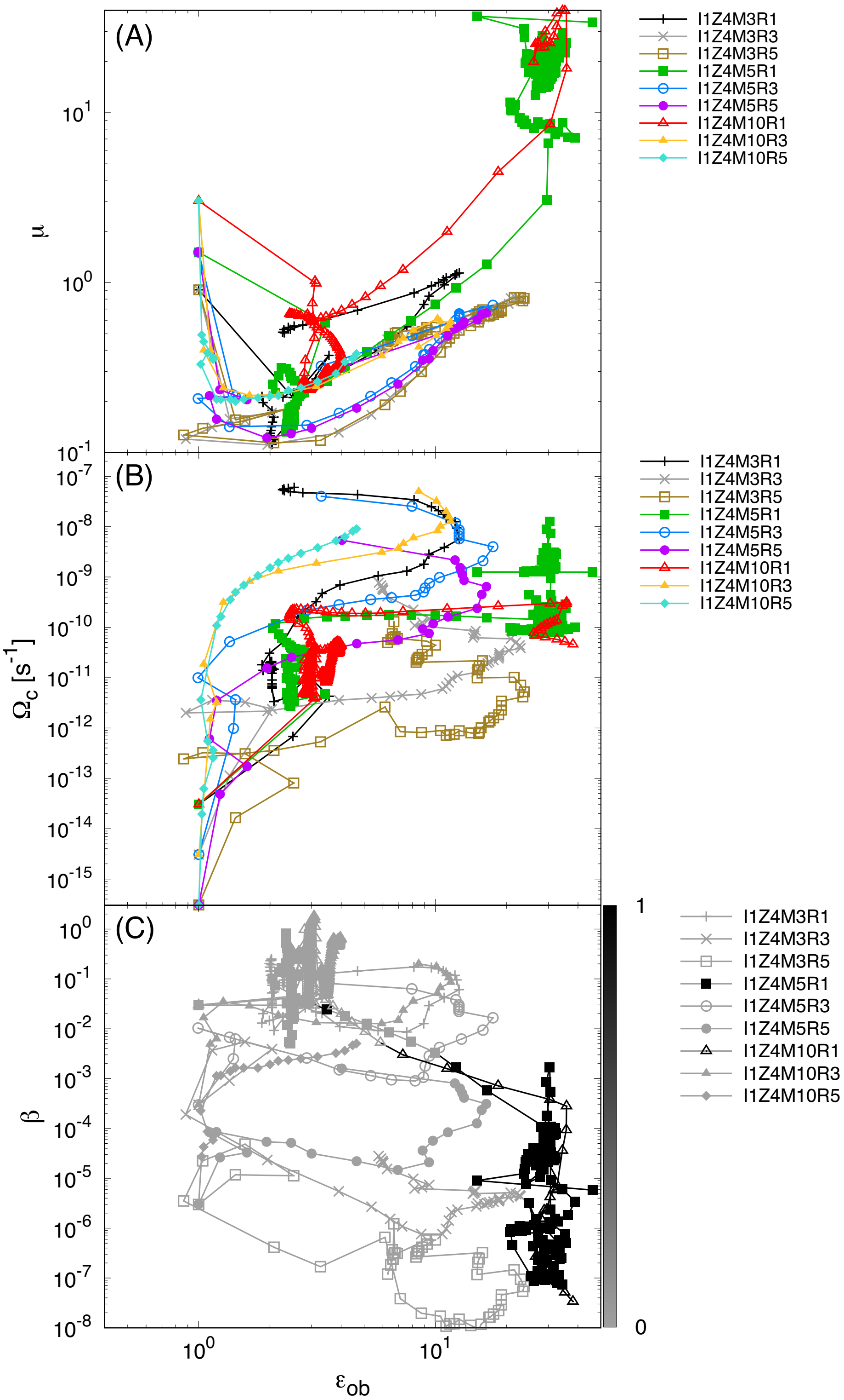

Figure 3.9: Same as Fig.3.4, but for model I1Z4 ($C_\zeta = 1$ and $Z/Z_\odot = 10^{-4}$)

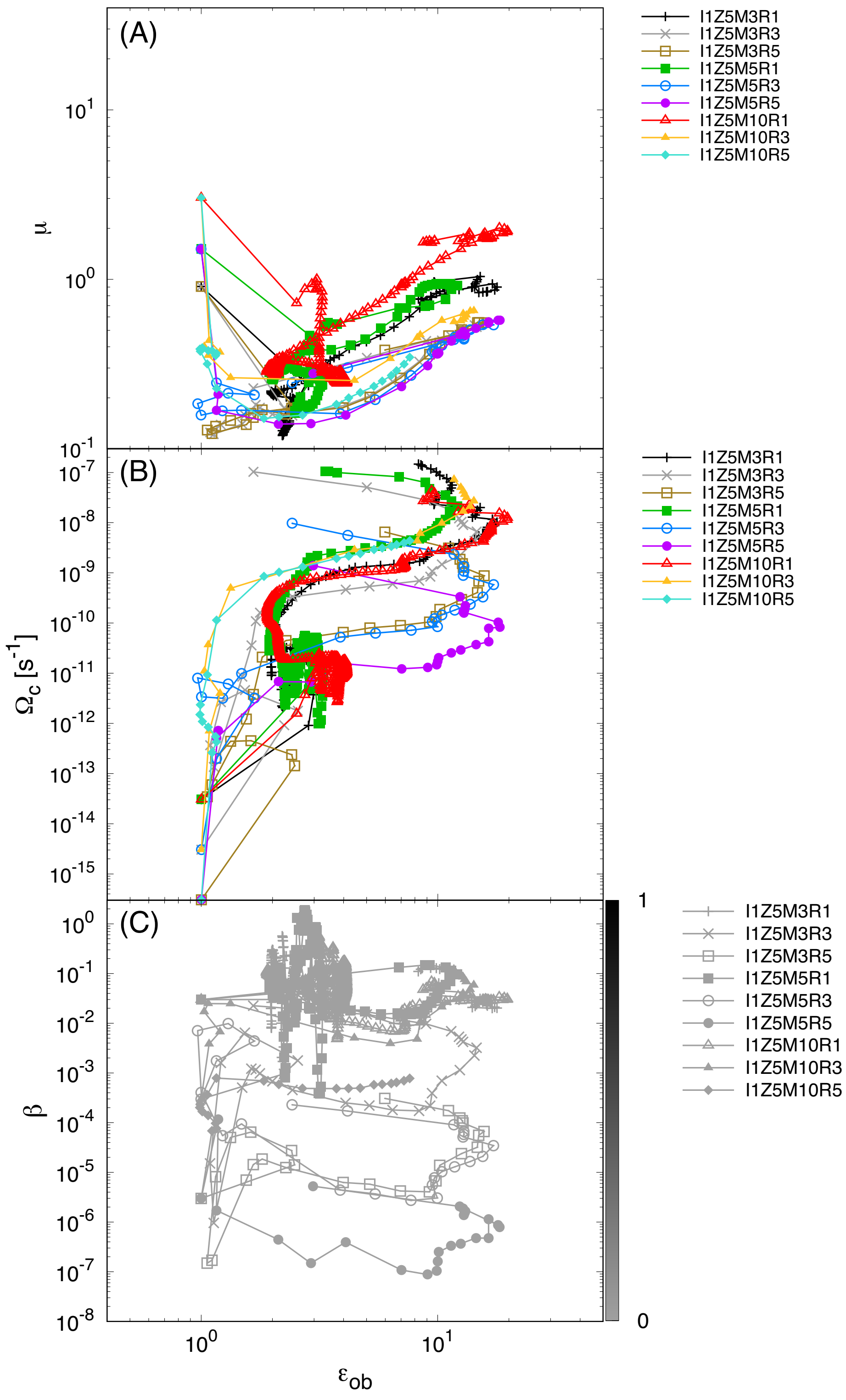

Figure 3.10: Same as Fig.3.4, but for model I1Z5 ($C_\zeta = 1$ and $Z/Z_\odot = 10^{-5}$)

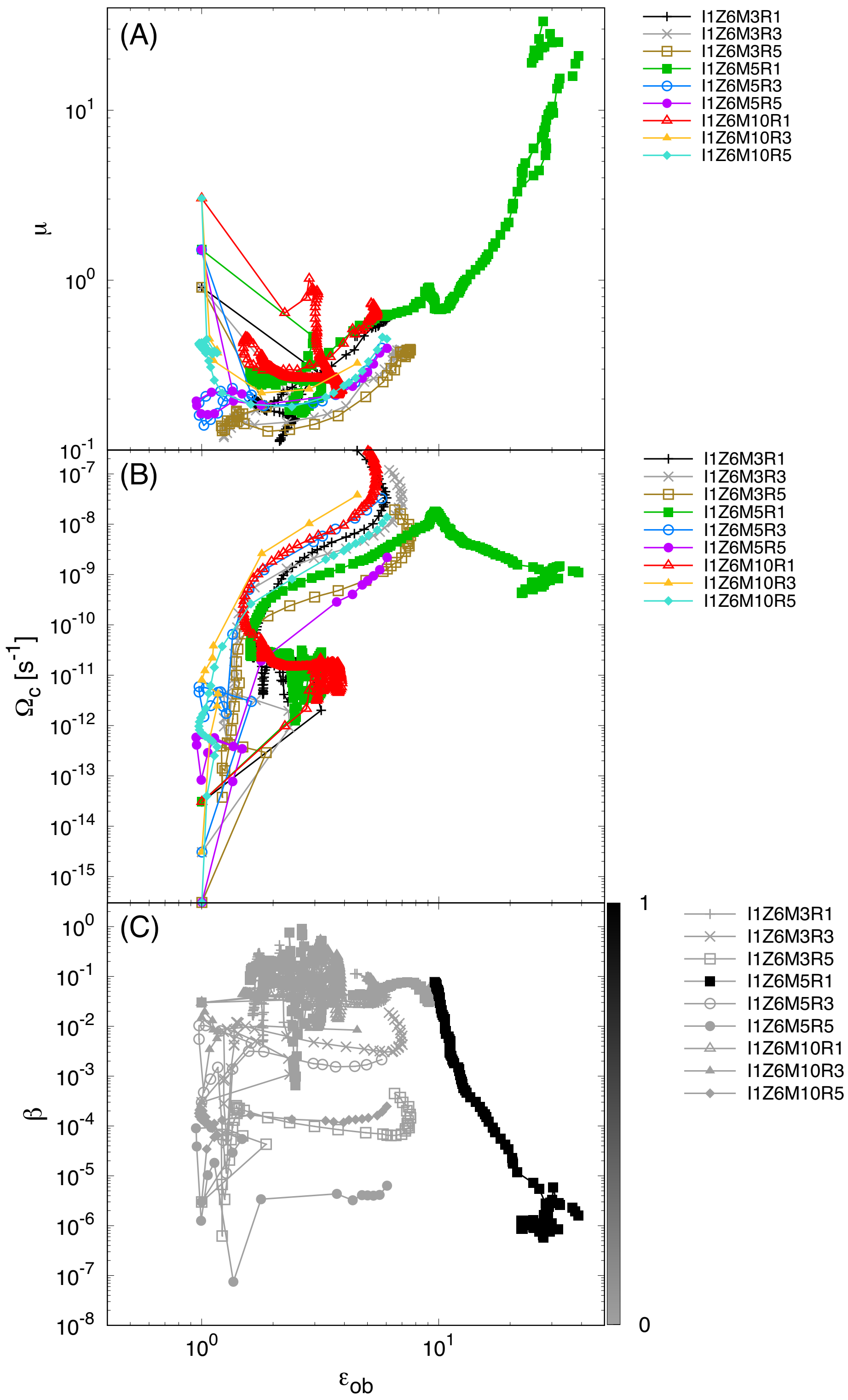

Figure 3.11: Same as Fig.3.4, but for model I1Z6 ($C_\zeta = 1$ and $Z/Z_\odot = 10^{-6}$)

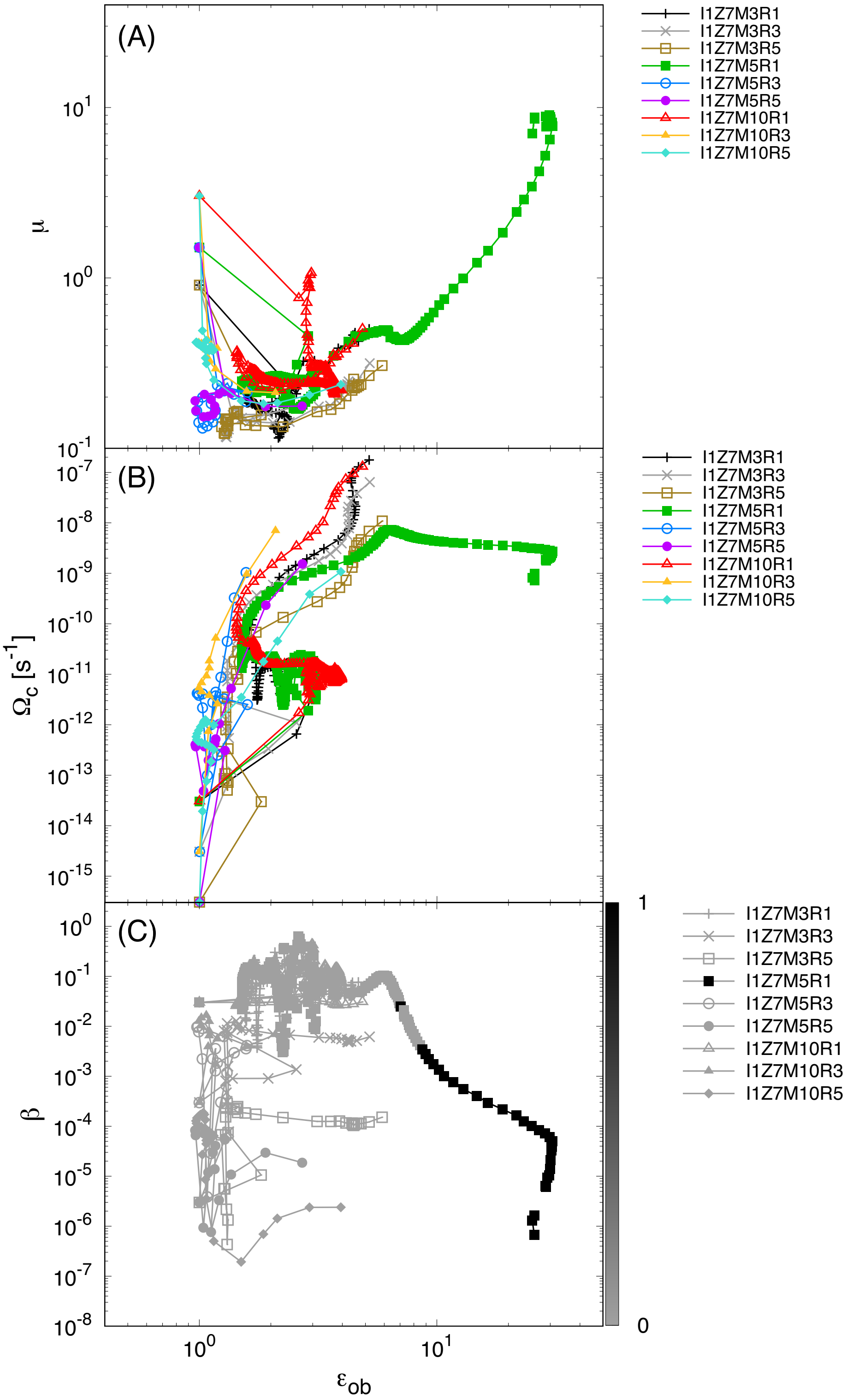

Figure 3.12: Same as Fig.3.4, but for model I1Z7 ($C_\zeta = 1$ and $Z/Z_\odot = 10^{-7}$)

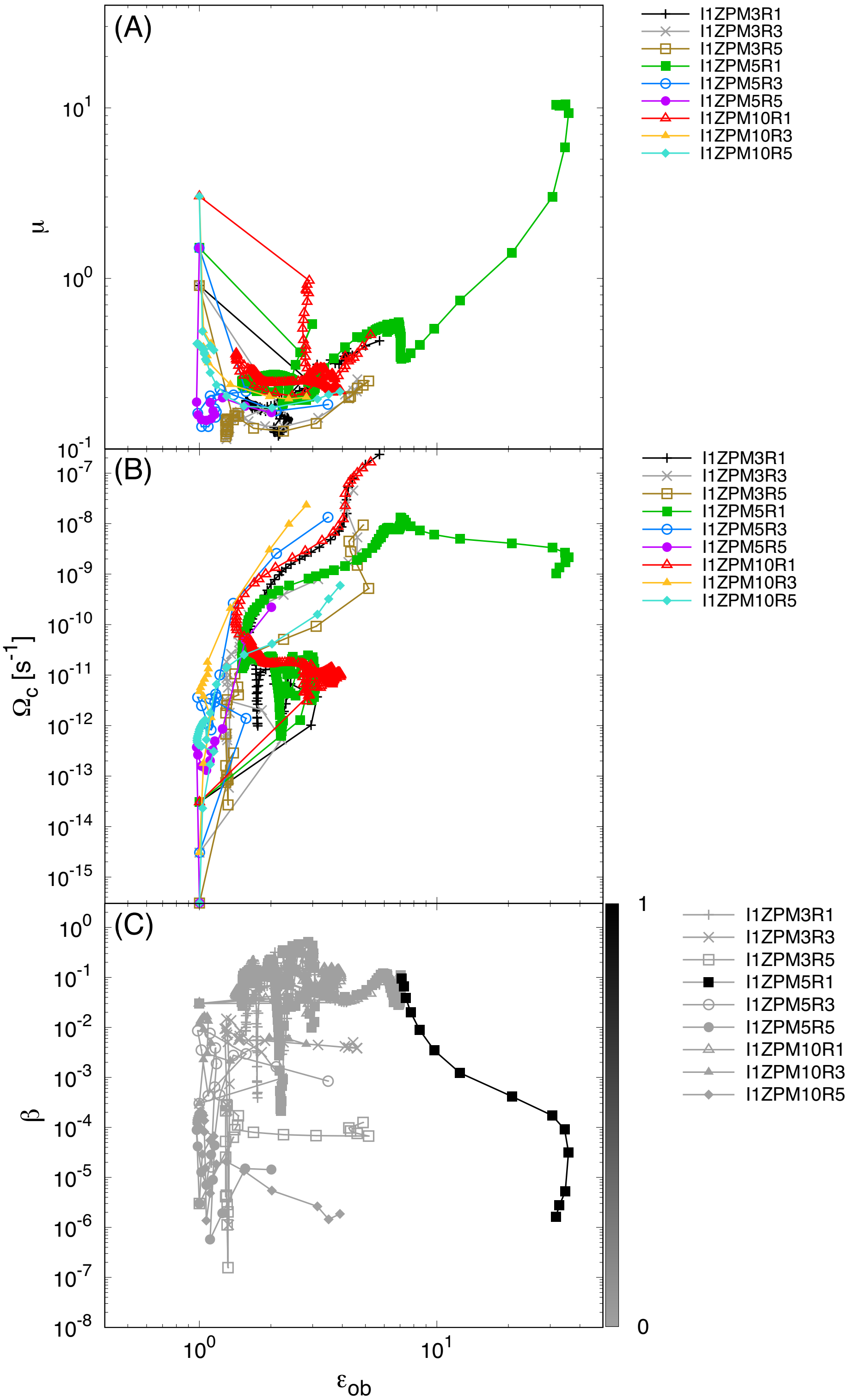

Figure 3.13: Same as Fig.3.4, but for model I1ZP ($C_\zeta = 1$ and $Z/Z_\odot = 0$)

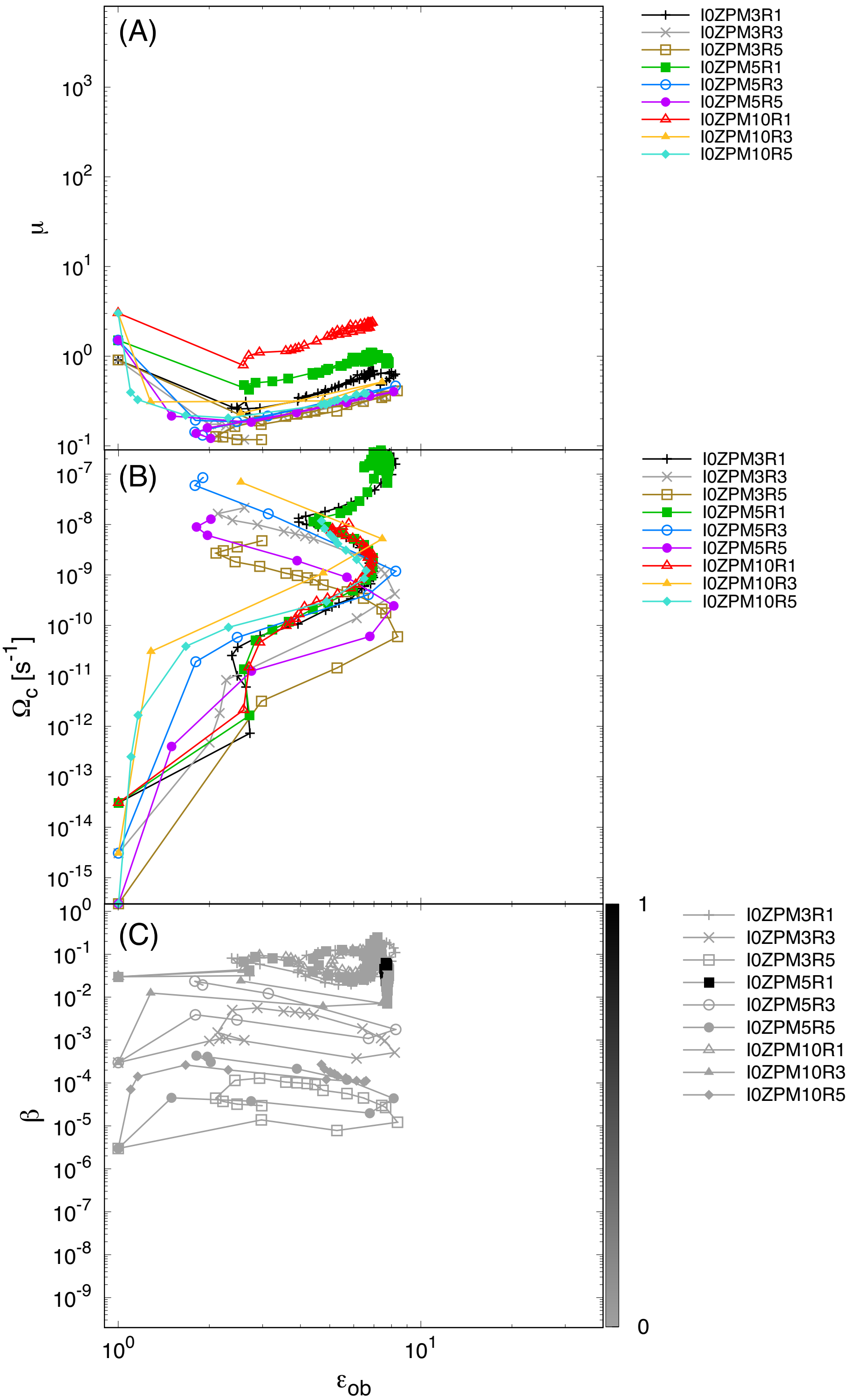

Figure 3.14: Same as Fig.3.4, but for model I0ZP ($C_\zeta = 0$ and $Z/Z_\odot = 0$)

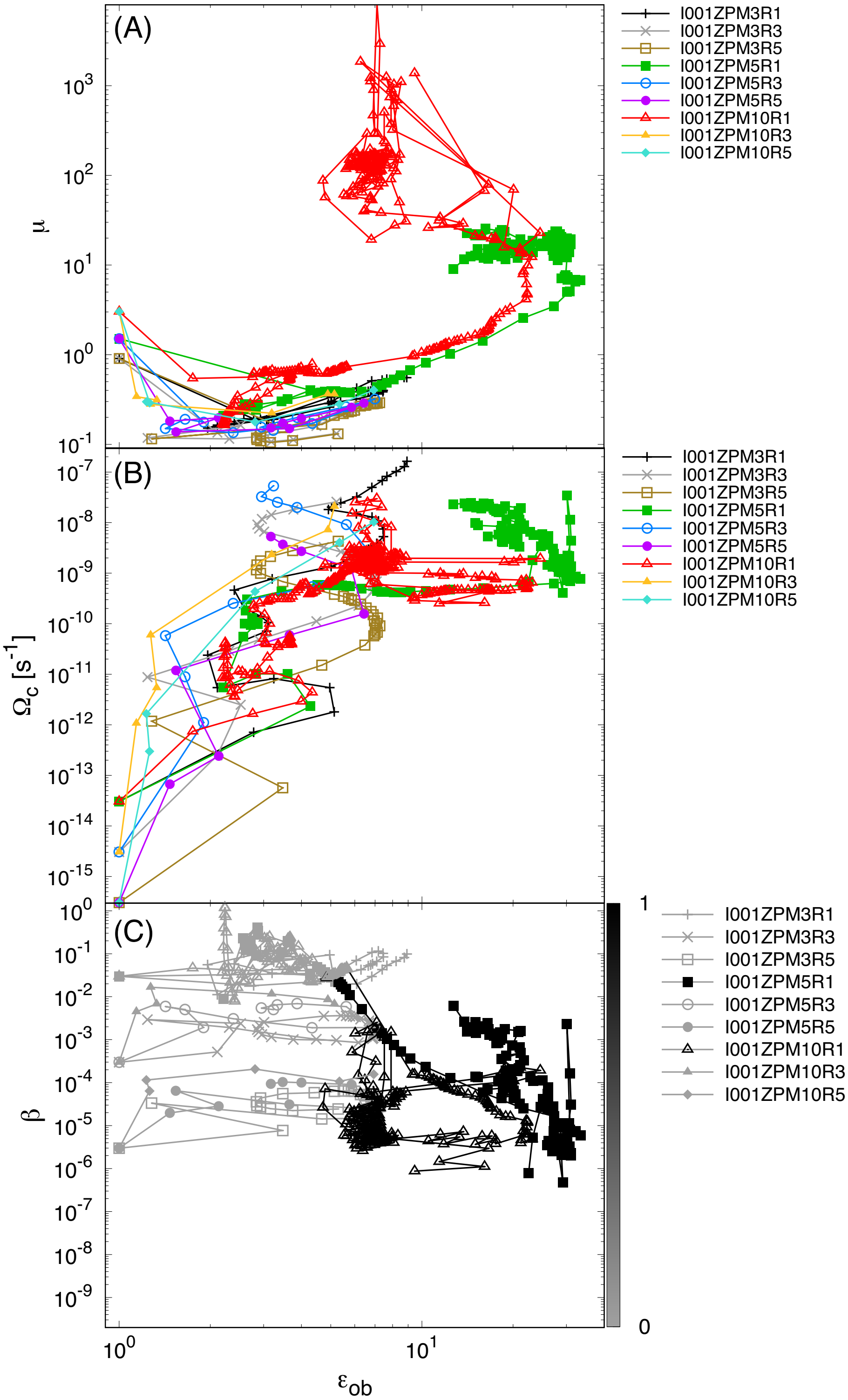

Figure 3.15: Same as Fig.3.4, but for model I001ZP ($C_\zeta = 0.01$ and $Z/\,Z_\odot = 0$)

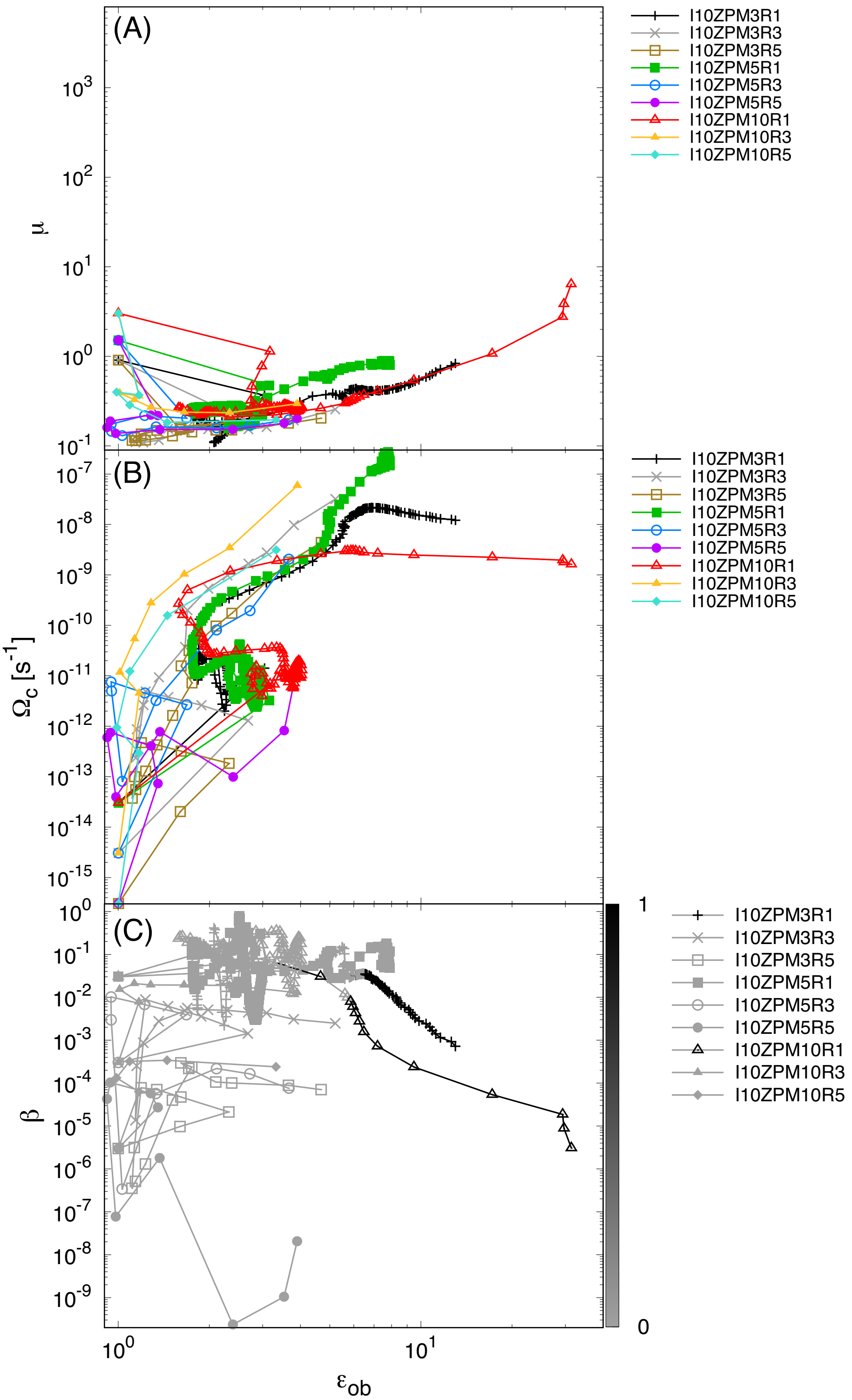

Figure 3.16: Same as Fig.3.4, but for model I10ZP ($C_\zeta = 10$ and $Z/Z_\odot = 0$)

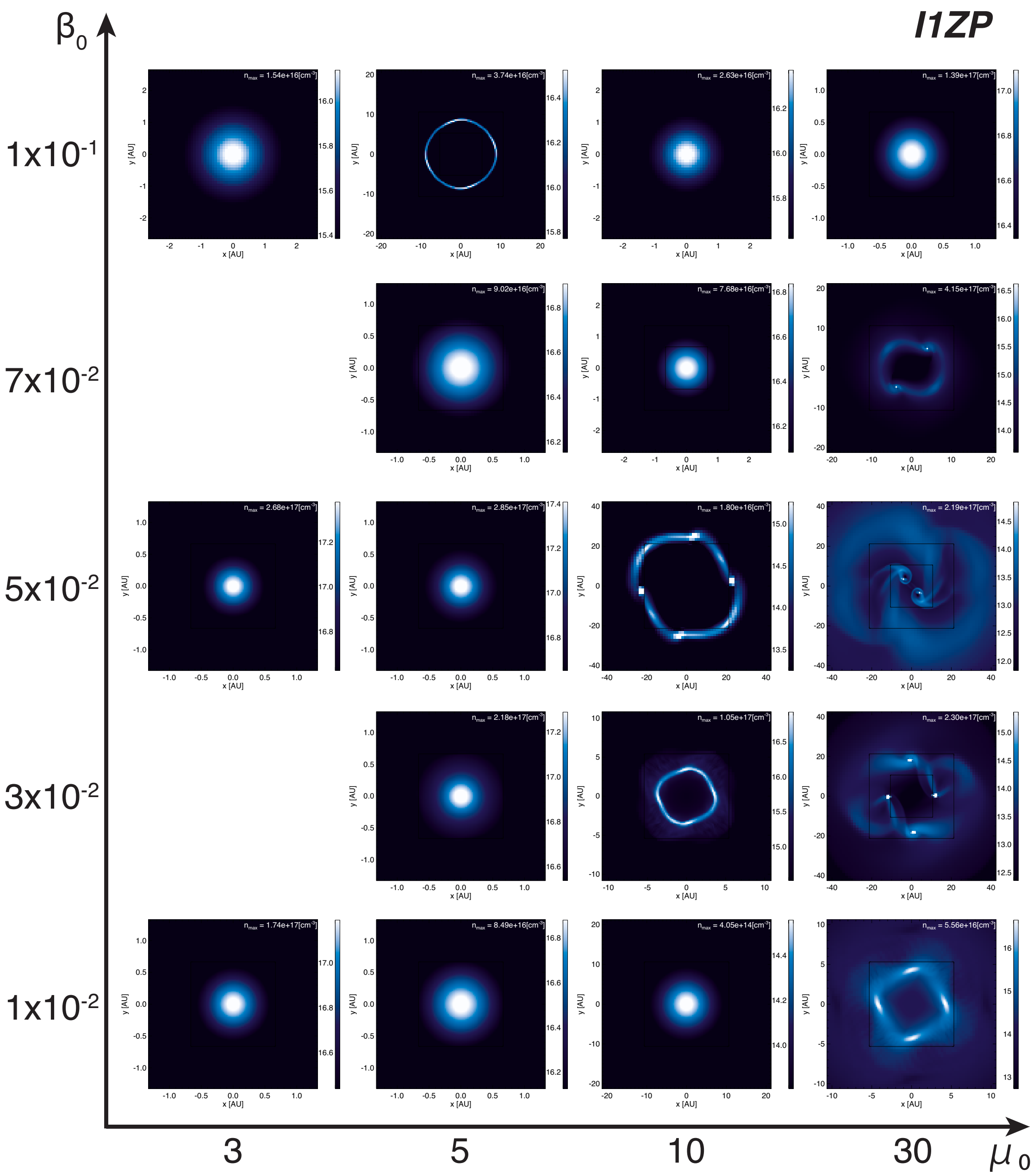

Figure 3.17: Plots of density distribution of each model with models arranged based on the ratio of rotational energy to gravitational energy β_0 (vertical axis) and the mass-to-flux ratio μ_0 (horizontal axis).

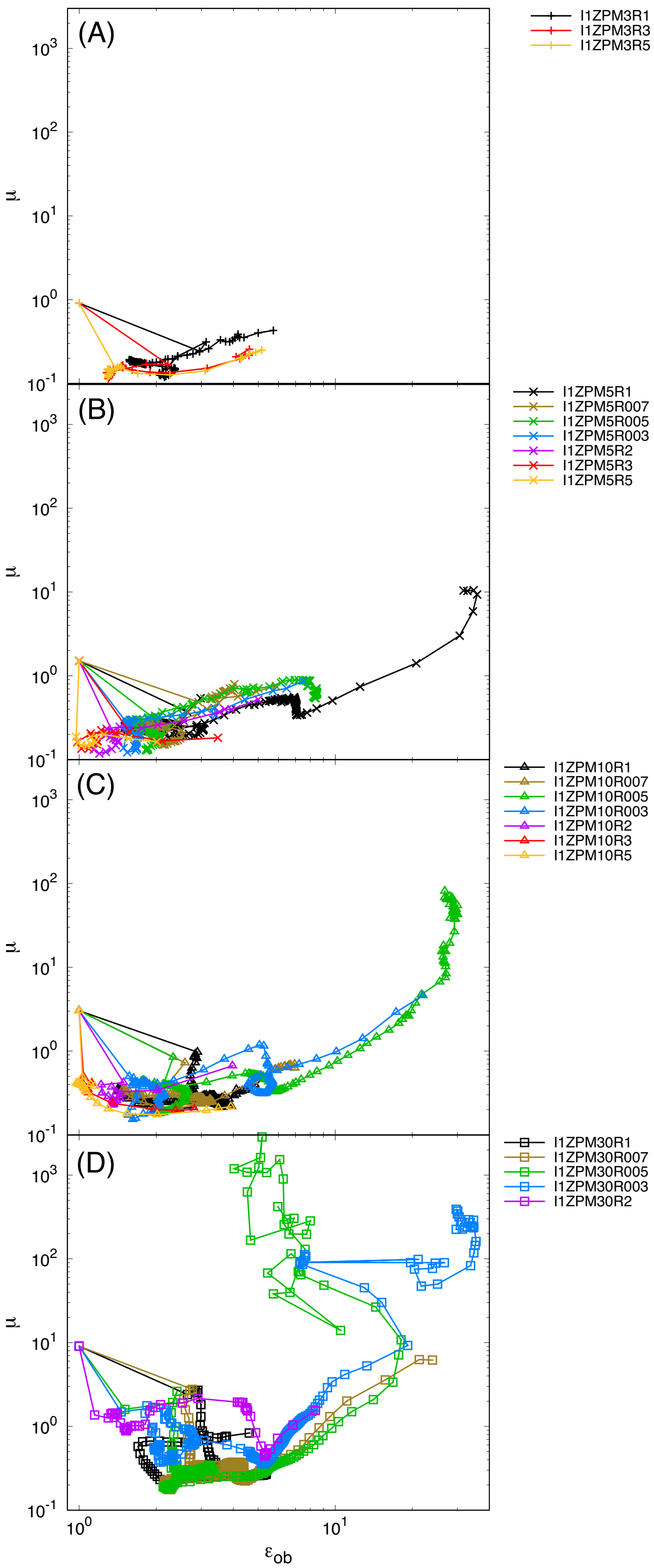

Figure 3.18: The results of model I1ZP ($C_\zeta = 1$ and $Z/Z_\odot = 0$). Mass-to-Flux ratio μ plotted against the oblateness of collapsing cloud with initial mass-to-flux ratio μ_0 of (A) 3, (B) 5, (C) 10, and (D) 30.

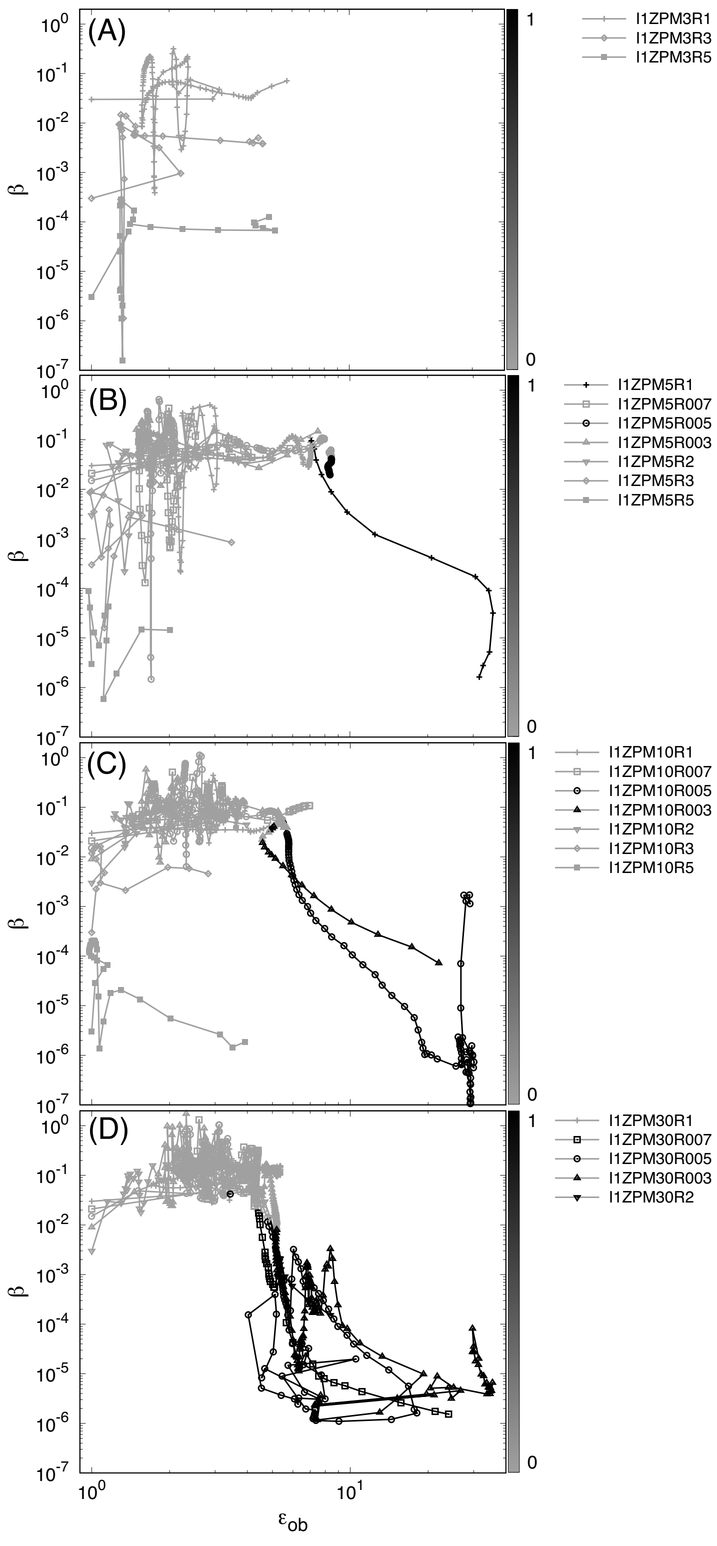

Figure 3.19: The ratio of rotational energy to gravitational energy β with respect to the oblateness of collapsing cloud for model I1ZP ($C_\zeta = 1$ and $Z/Z_\odot = 0$). Four panels show $\mu_0 =$ (A) 3, (B) 5, (C) 10, and (D) 30. Displayed in black when the $\rho_{\max}$ value is 10 or more times the central density value.

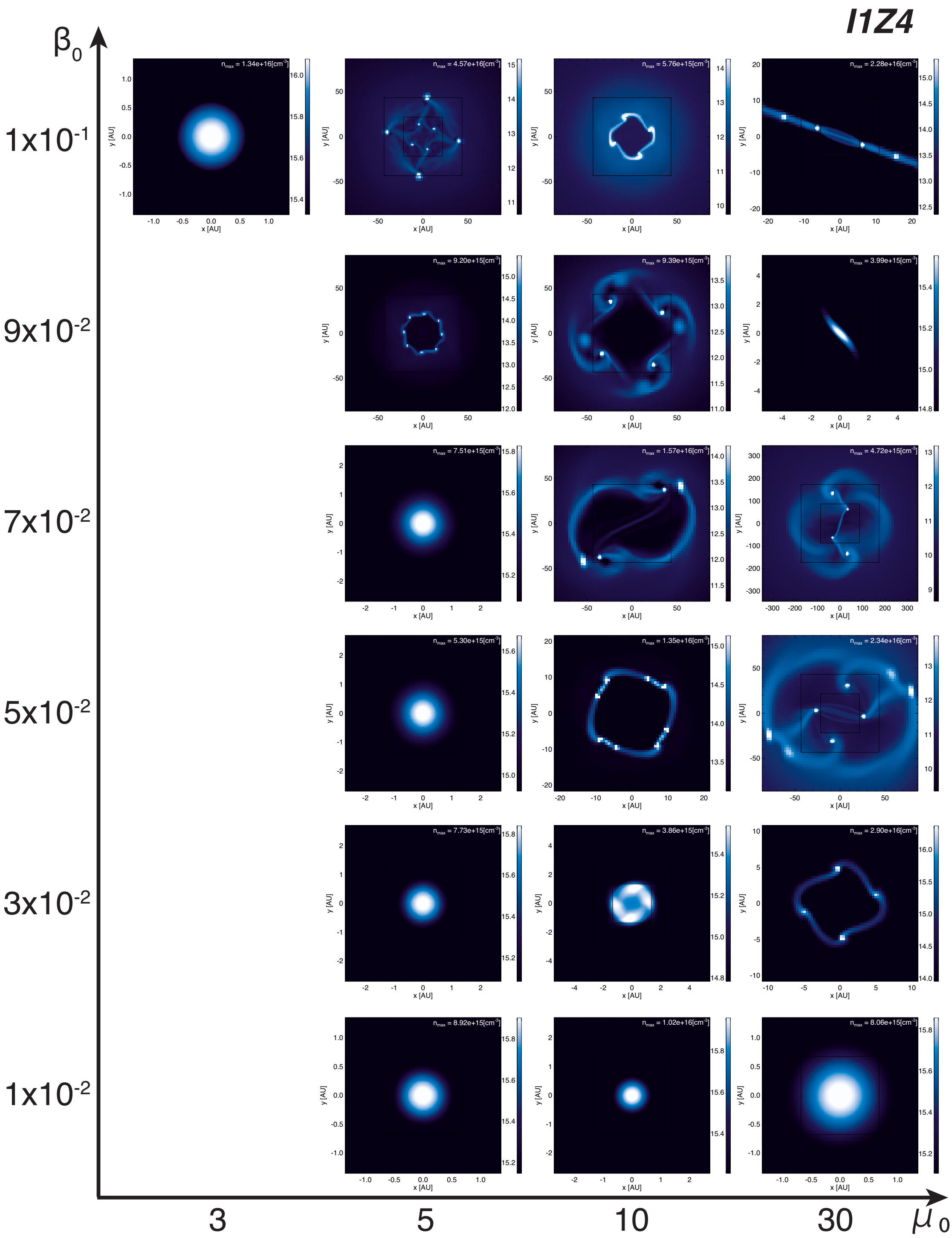

Figure 3.20: Same as Fig.3.17, but for model I1Z4 ($C_\zeta = 1$ and $Z/Z_\odot = 10^{-4}$)

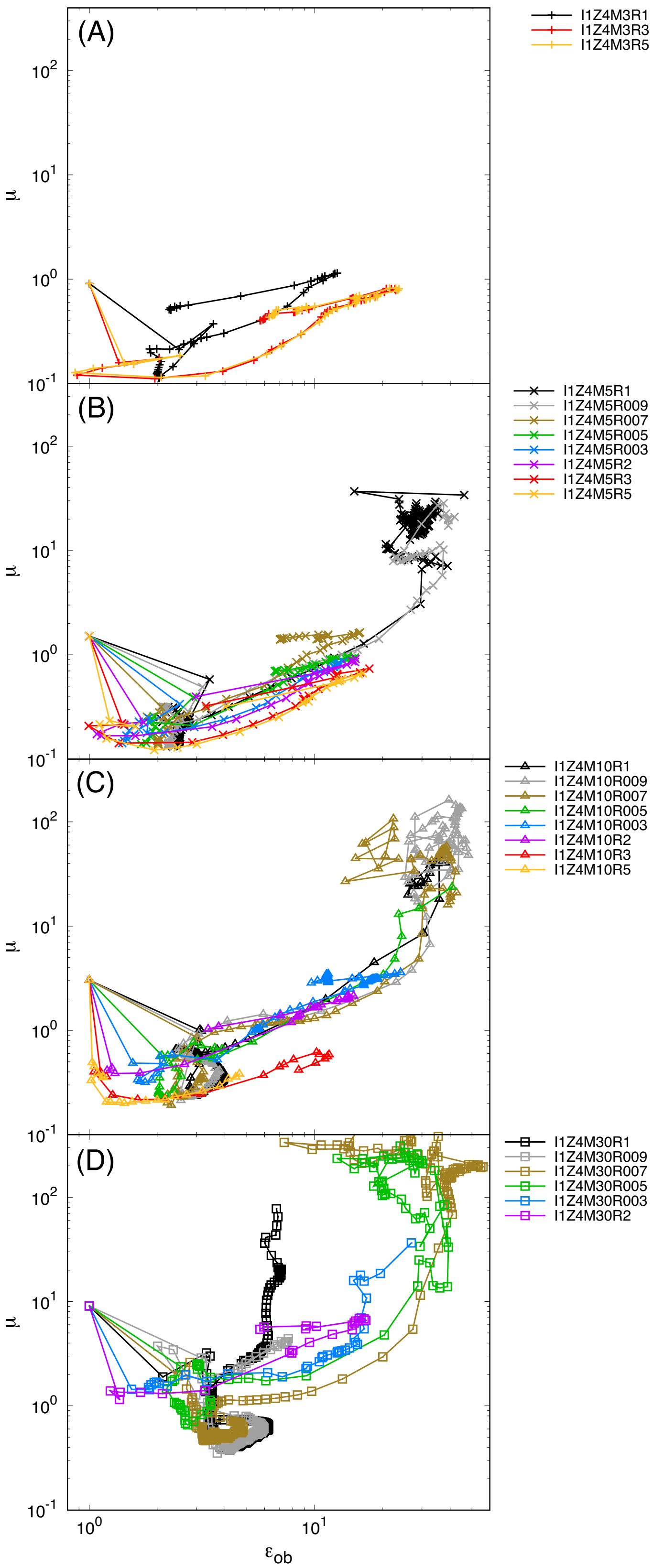

Figure 3.21: Same as Fig.3.18, but for model I1Z4 ($C_\zeta = 1$ and $Z/Z_\odot = 10^{-4}$)

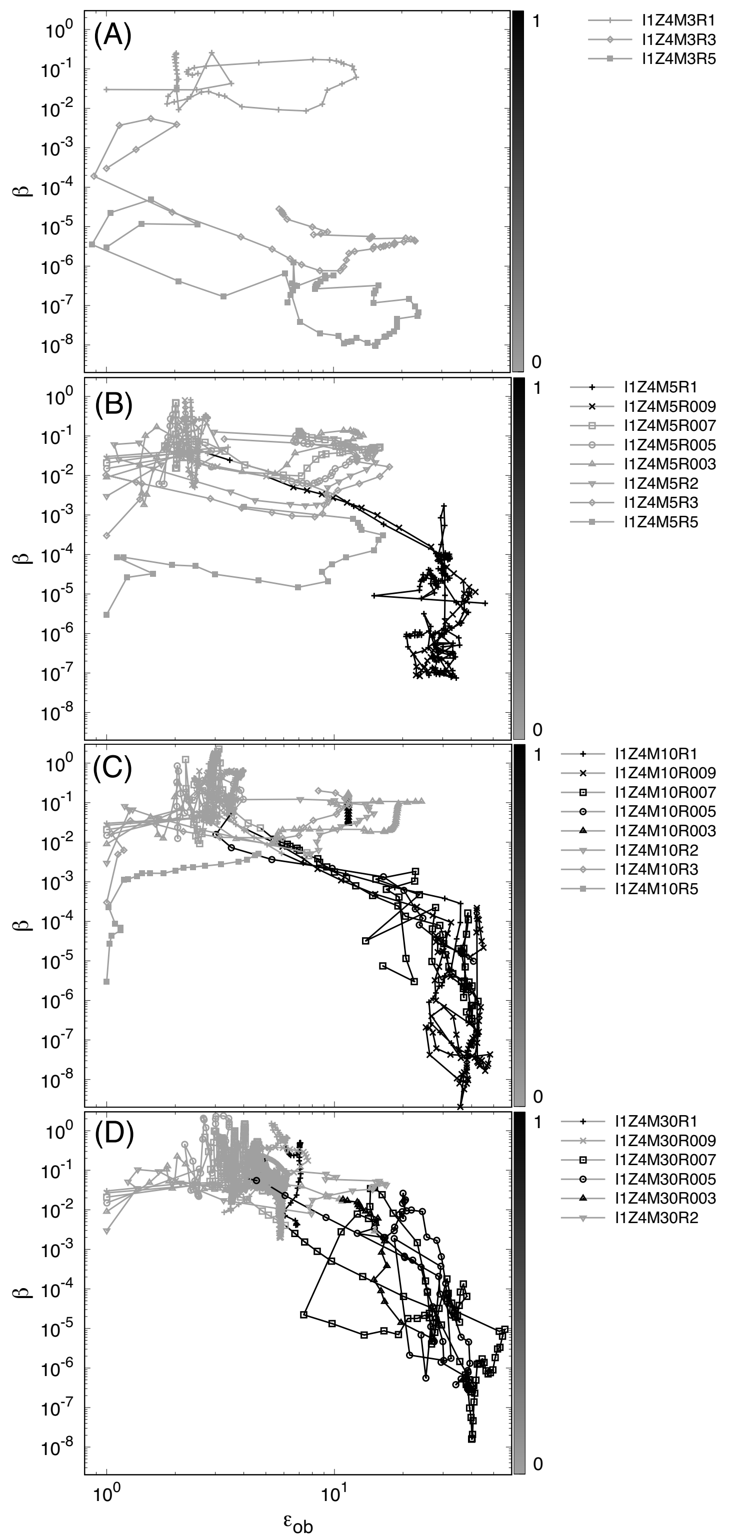

Figure 3.22: Same as Fig.3.19, but for model I1Z4 ($C_\zeta = 1$ and $Z/Z_\odot = 10^{-4}$)

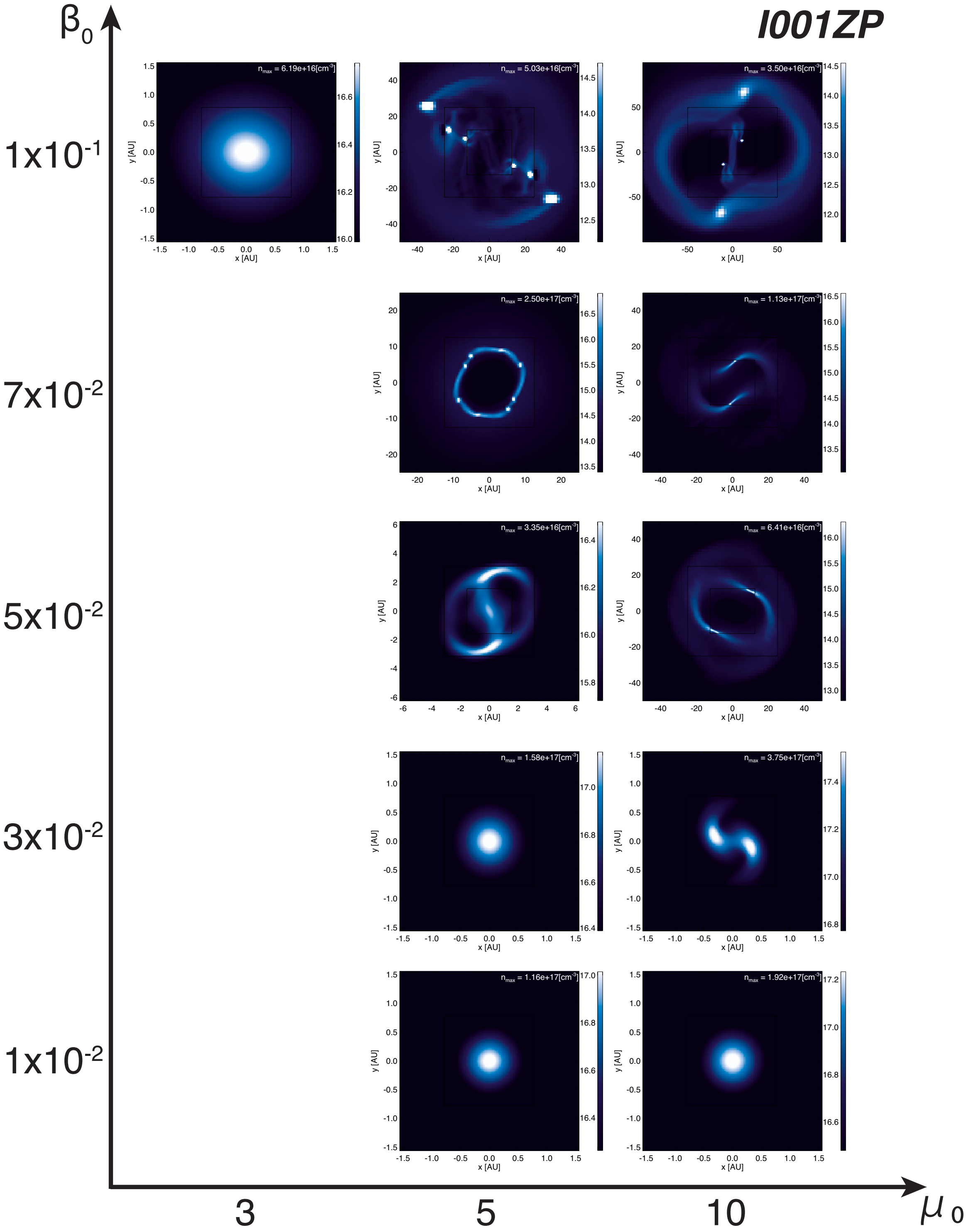

Figure 3.23: Same as Fig.3.17, but for model I001ZP ($C_\zeta = 0.01$ and $Z/Z_\odot = 0$)

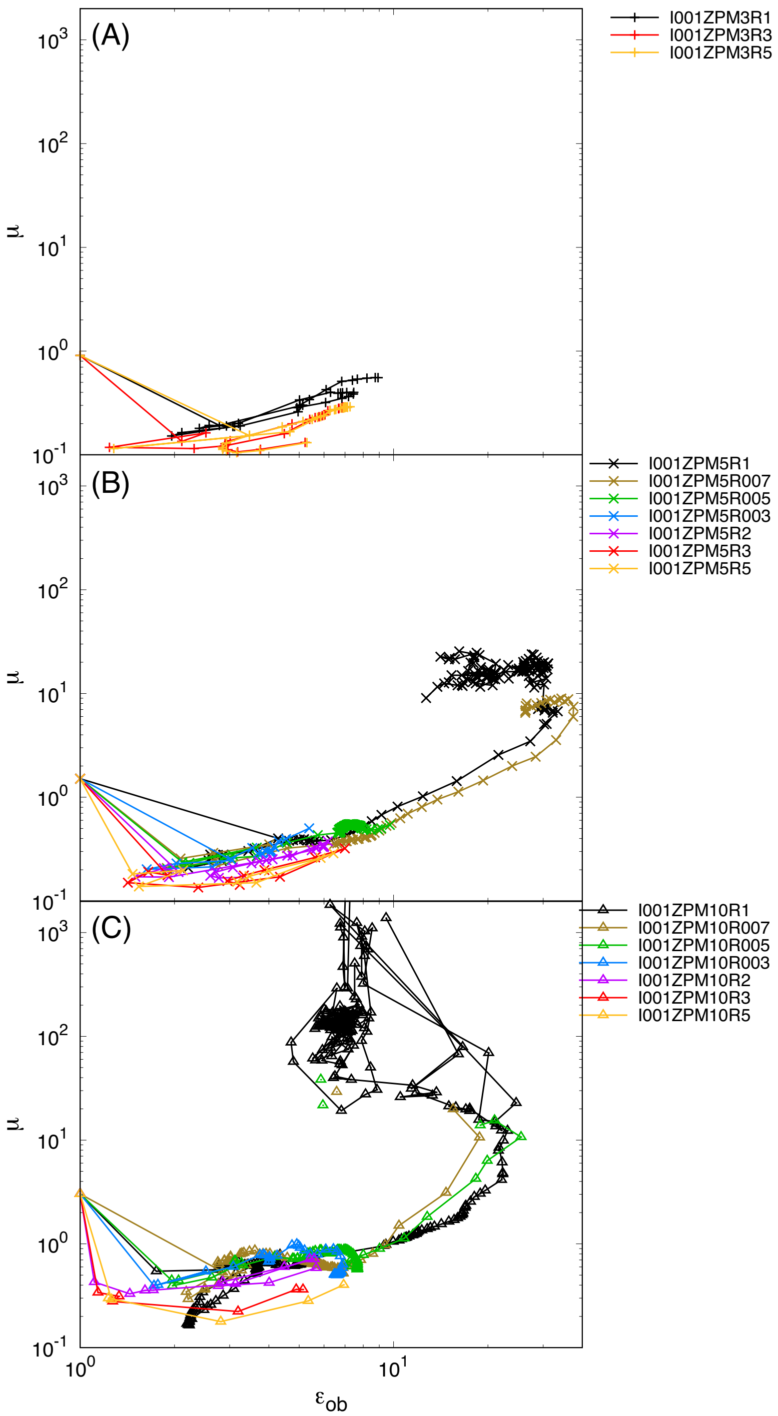

Figure 3.24: The results of model I001ZP ($C_\zeta = 1$ and $Z/\,Z_\odot = 0$). Mass-to-Flux ratio μ plotted against the oblateness of collapsing cloud with initial mass-to-flux ratio μ_0 of (A) 3, (B) 5, and (C) 10

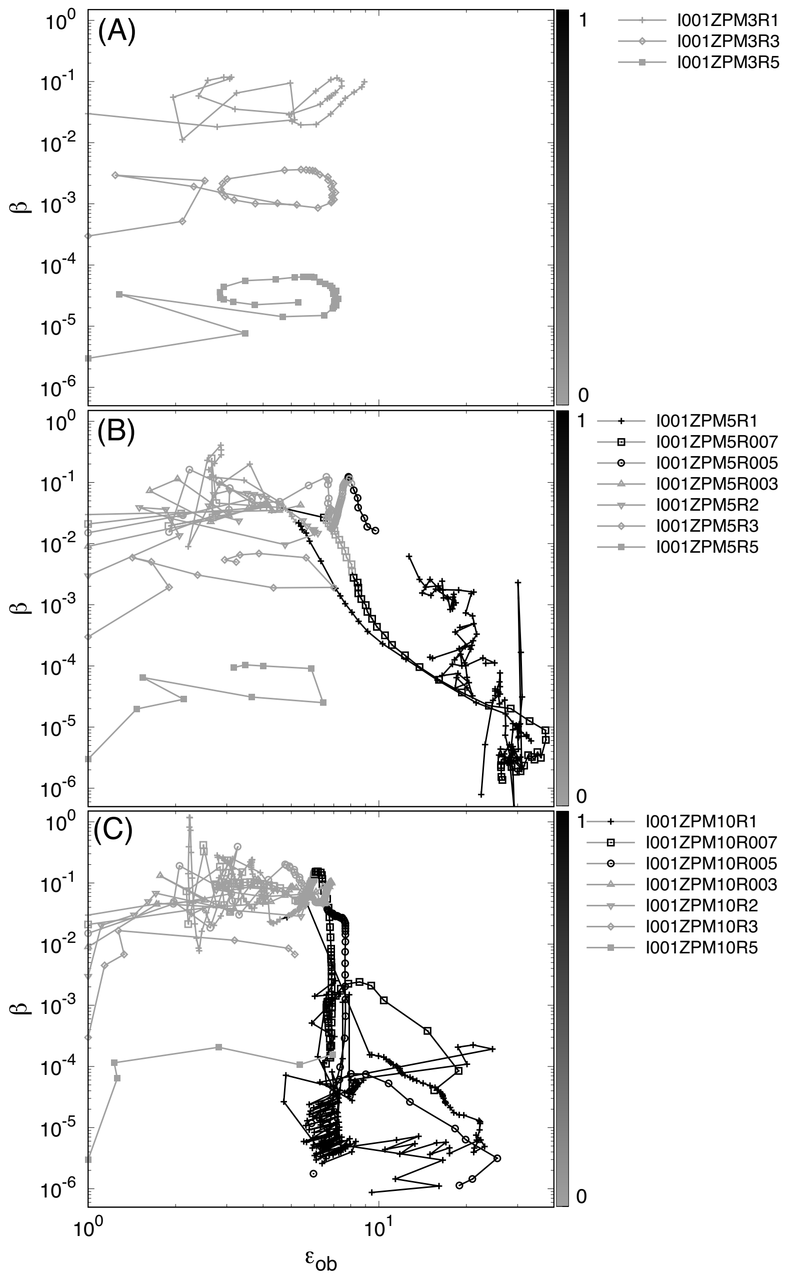

Figure 3.25: The ratio of rotational energy to gravitational energy β with respect to the oblateness of collapsing cloud for model I001ZP ($C_\zeta = 0.01$ and $Z/Z_\odot = 0$). Three panels show $\mu_0 =$ (A) 3, (B) 5, and (C) 10. Displayed in black when the $\rho_{\rm max}$ value is 10 or more times the central density value.

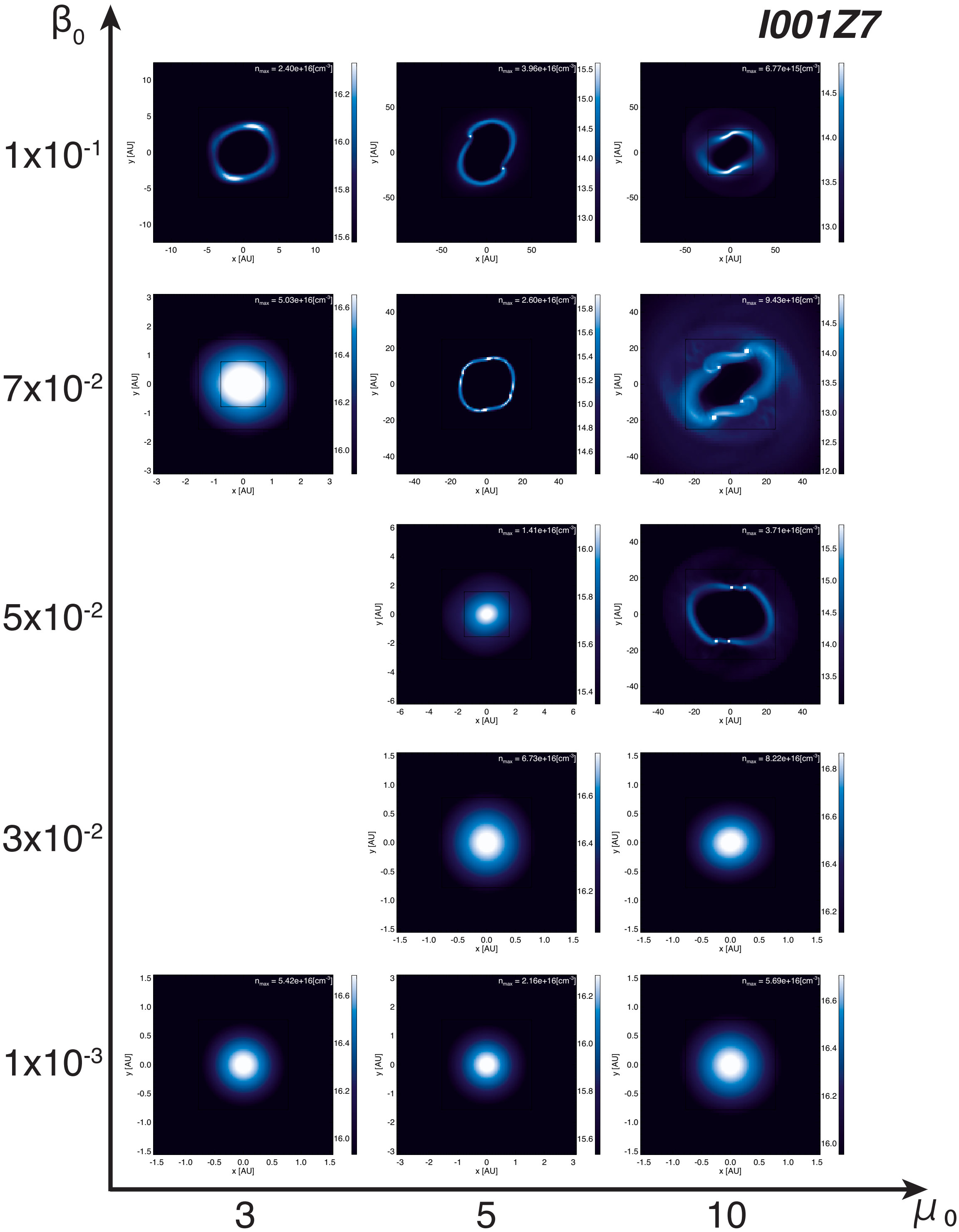

Figure 3.26: Same as Fig.3.17, but for model I001Z7 ($C_\zeta = 0.01$ and $Z/Z_\odot = 10^{-7}$)

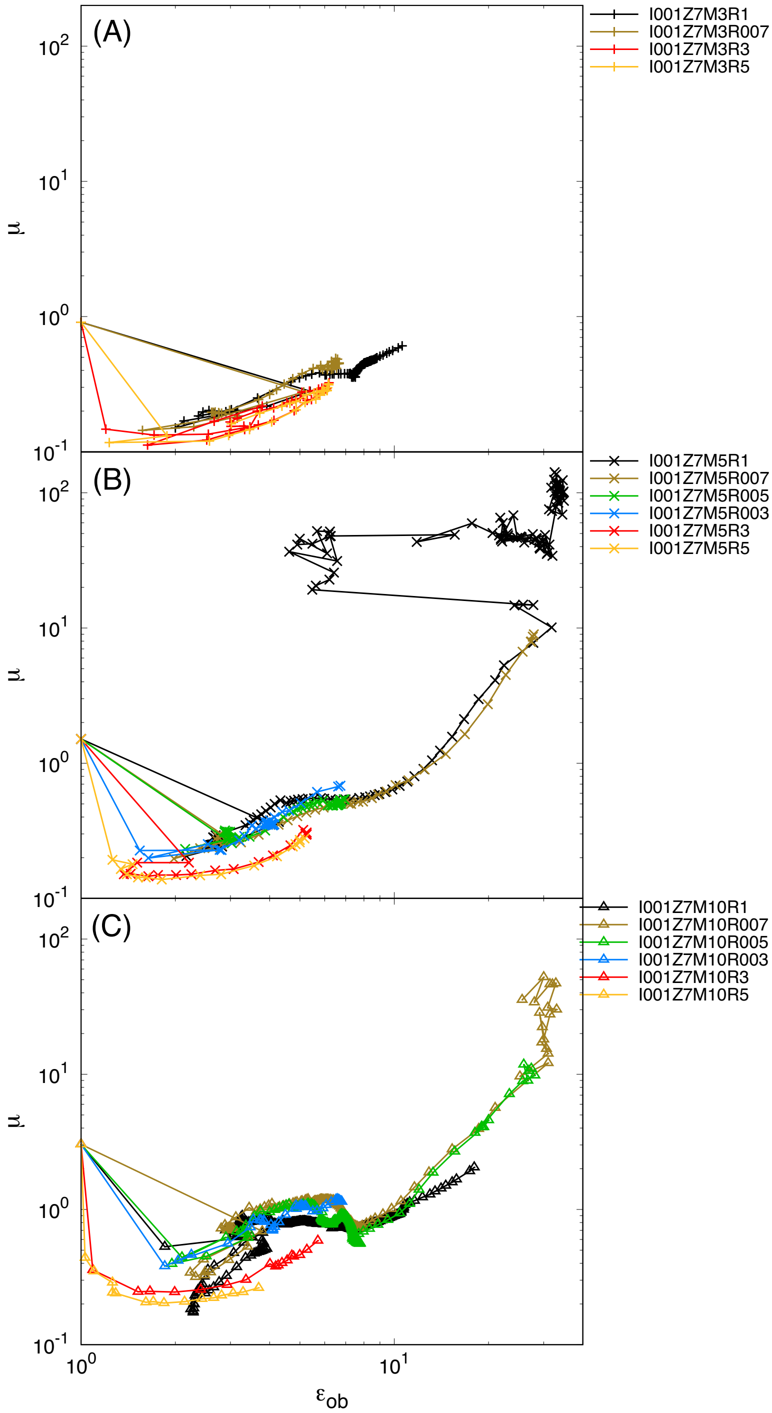

Figure 3.27: Same as Fig.3.24, but for model I001Z7 ($C_\zeta = 0.01$ and $Z/Z_\odot = 10^{-7}$)

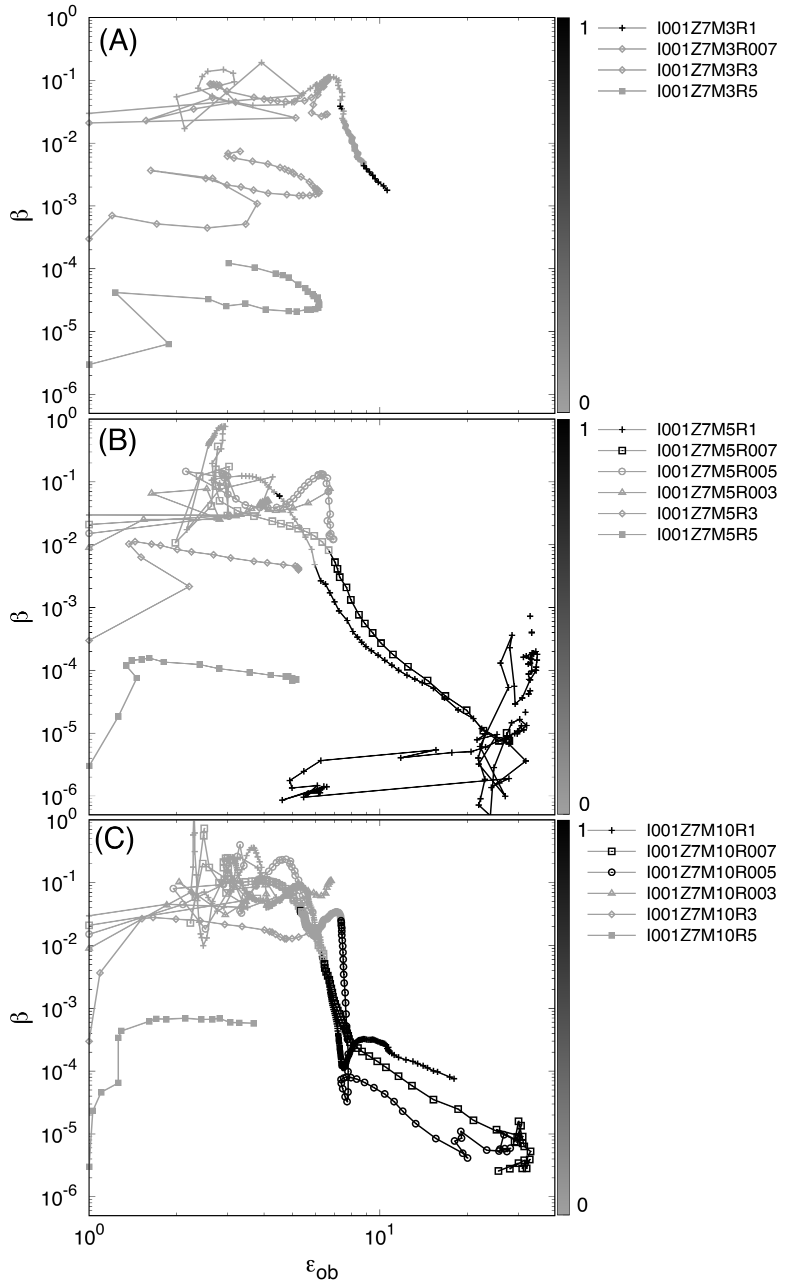

Figure 3.28: Same as Fig.3.25, but for model I001Z7 ($C_\zeta = 0.01$ and $Z/Z_\odot = 10^{-7}$)

Chapter 4

SUMMARY

There are various star-forming environments in the universe, such as our galaxy, starburst galaxy, first galaxy and so on. Star formation process would depend on the nature of the environment, in such a diverse environment, various star formation processes are considered. Therefore, the star formation process is expected to vary from environment to environment. One important issue is the stellar multiplicity, because the stellar mass changes according to the number of stars. Furthermore, Dynamical, radiative and chemical feedbacks to the surroundings are strongly depend on the stellar mass (e.g., Baraffe et al. 2001, Heger and Woosley 2002, Latif and Khochfar 2019). The observational studies have predicted that 60 to 80% of the field stars are binary or multiple system in our galaxy (Duquennoy and Mayor 1991). On the other hands, the metal-poor stars, especially the CEMP-no stars, are observed as binary with about 40% probability (Arentsen et al. 2019). It will take more than a few years to increase the number of metal-poor stars. Therefore, it is important to examine the binary/multiplicity formation rate in the early universe environment from theoretical studies.

In the present study, I considered 32 different star-forming environments in combination with $Z = 0,\ 10^{-7},\ 10^{-6},\ 10^{-5},\ 10^{-4},\ 10^{-3},\ 10^{-2},\ 10^{-1}\ Z_{\odot}$ and $C_{\zeta} = 0,\ 0.01,\ 1,\ 10$, and prepared clouds having different mass-to-flux ratios μ_0 and ratios of rotational energy to gravitational energy β_0. I investigated the fragmentation condition in various star-forming environments. In the present study, we performed 334 calculations in total and obtained the following results:

1. There is a difference in the fragmentation process depending on the combination of the ionization parameter C_ζ and the metallicity $Z/\,Z_\odot$ in collapsing cloud environment. As metallicity and ionization strength increase, the number of models showing fragmentation increases. The gas cooling becomes effective clearly depends on them, and it makes the cloud flat. In addition, if the amount of metal is large, the energy released by the contraction cannot be escaped from inner region to the outside and the adiabatic core is formed before the protostar formation. This core is in a quasi-hydrostatic state, thus, it slowly contracts. Since the gas with a large angular momentum accretes from the envelope to the core, fragmentation is promoted.

2. In general, a model with a higher β_0 and μ_0 shows fragmentation. Depending on the environment, if the magnetic field strength is strong and the rotation is fast, angular momentum is efficiently transported to the outside by the outflow and the magnetic breaking. As a result, the fragmentation is less likely to occur. The fragmentation can occur in the range of $\beta_0 \geq 10^{-3}$ and $\mu_0 \geq 3$. Furthermore, with additional calculations, if the range of $\beta_0 \geq 3.0 \times 10^{-2}$ and $\mu_0 \geq 10$ are given to the initial state, fragmentation occurs in any environment.

3. The cloud rotation and magnetic field affect the dynamics of the gas cloud. Therefore, focusing on the oblateness of cloud, the magnetic field and the rotation of cloud, I estimated the fragmentation condition. The calculation showed $\epsilon_{\rm ob} \geq 5$, $\mu \geq 0.6 - 1.0$, and $\beta \geq 10^{-2}$ are necessary for the fragmentation to occur. However, there are non-fragmentation models that are in this parameter range before the end of the simulation. These models are likely to fragment in a farther evolutional stage and become close binary system. Furthermore, if these binaries gain a lot of mass and grow into a massive star binary, it can be the origin of the binary black hole.

Appendix A

Thermal evolution for $C_\zeta = 0.01$ and 10

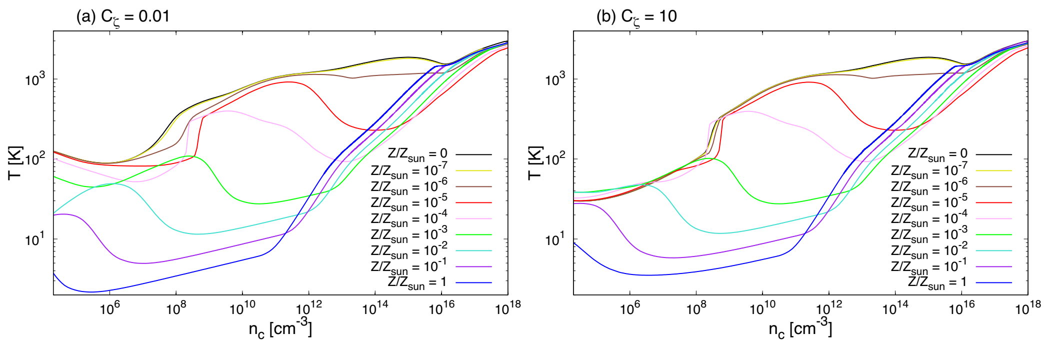

Figure A.1: Thermal evolution for $C_\zeta = 0.01$ and 10. Temperature are plotted with respect to the central number density (a) $C_\zeta = 0.01$ and (b) 10. Higuchi et al. (2018) shows only the results for $C_\zeta = 0$ and 1, so it is shown here.

Appendix B

Magnetic evolution for $C_\zeta = 0.01$ and 10

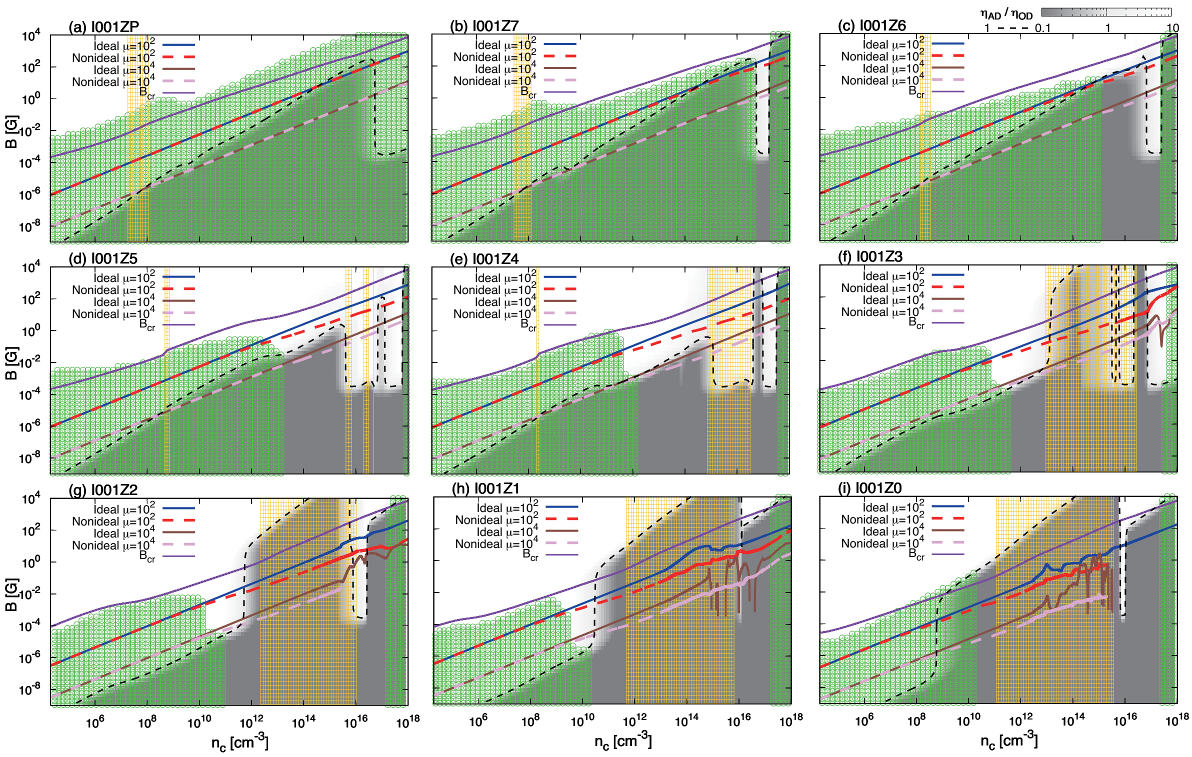

Figure B.1: Higuchi et al. (Same as Fig.8 in 2018), but for models with $C_\zeta = 0.01$.

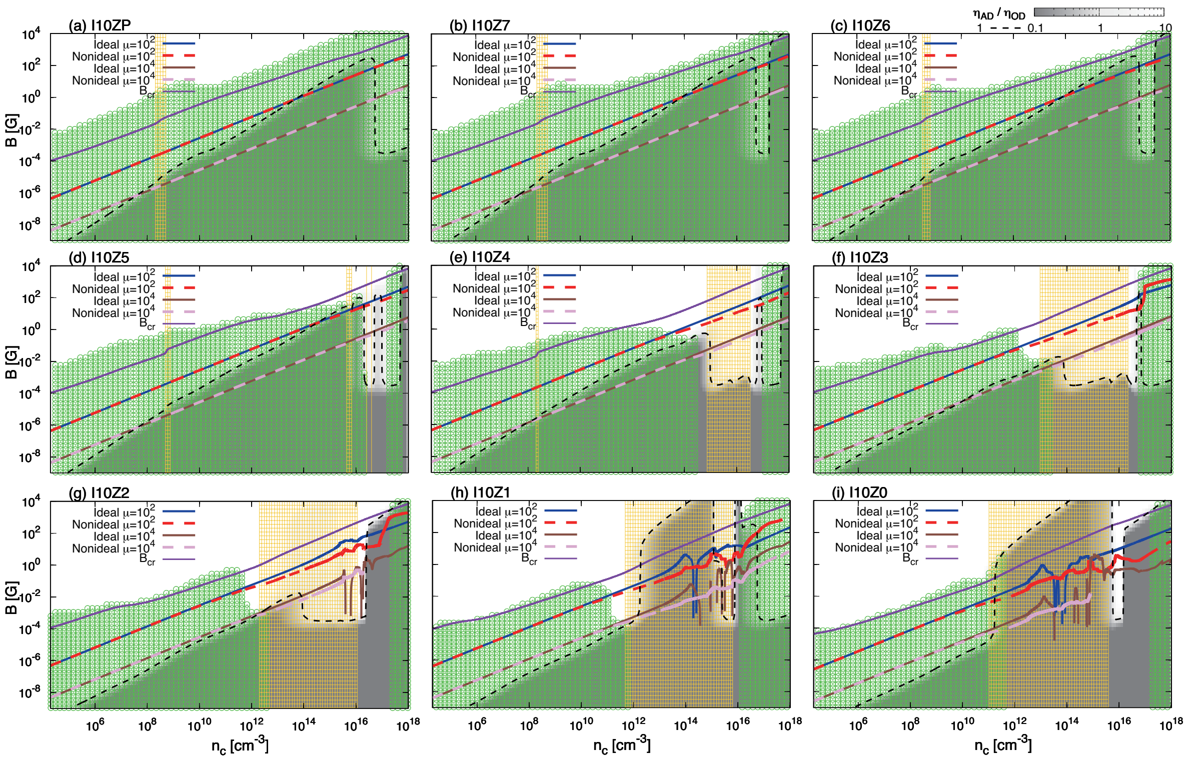

Figure B.2: Higuchi et al. (Same as Fig.8 in 2018), but for models with $C_\zeta = 10$.

ACKNOWLEDGEMENTS

Foremost, I wish to thank my supervisor, Associate Professor Masahiro Machida, for many supports to perform my researchs and for seminars to my study. I am also thankful to Professor Hajime Susa for his encouragement and comments. I would also like to thank Professor Minoru Sekiya and Assistant Professor Kensuke Nakajima for their continuous encouragements and advices. I also thank everyone for many useful comments on my research.

The present research used the computational resources of the HPCI system provided by (Cyber Sciencecenter, Tohoku University; Cybermedia Center, Osaka University, Earth Simulator, JAMSTEC) through the HPCI System Research Project (Project ID:hp160079, hp170047,hp180001, hp190035). Simulations reported in this paper were also performed by 2017 Koubo Kadai on Earth Simulator (NEC SX-ACE) at JAMSTEC. This work was partly achieved through the use of supercomputer system SX-ACE at the Cyber- media Center, Osaka University. Simulations were also performed by 2018 Koubo Kadai on Earth Simulator (NEC SX-ACE) at JAMSTEC.

Bibliography

Abel, Tom, Greg L. Bryan, and Michael L. Norman. 2002. The Formation of the First Star in the Universe. *Science* 295:93–98.

Arentsen, A., E. Starkenburg, M. D. Shetrone, K. A. Venn, É. Depagne, and A. W. McConnachie. 2019. Binarity among CEMP-no stars: an indication of multiple formation pathways? *Astronomy & Astrophysics* 621:A108.

Banerjee, Robi, and Ralph E. Pudritz. 2006. Outflows and Jets from Collapsing Magnetized Cloud Cores. *the Astrophysical Journal* 641:949–960.

Baraffe, I., A. Heger, and S. E. Woosley. 2001. On the Stability of Very Massive Primordial Stars. *the Astrophysical Journal* 550:890–896.

Basu, Shantanu, and Telemachos Ch. Mouschovias. 1994. Magnetic Braking, Ambipolar Diffusion, and the Formation of Cloud Cores and Protostars. I. Axisymmetric Solutions. *the Astrophysical Journal* 432:720.

Beers, Timothy C., and Norbert Christlieb. 2005. The Discovery and Analysis of Very Metal-Poor Stars in the Galaxy. *Annual Review of Astronomy and Astrophysics* 43:531–580.

Bonnor, W. B. 1956. Boyle's Law and gravitational instability. *Monthly Notices of the Royal Astronomical Society* 116:351.

Bouwens, R. J., G. D. Illingworth, I. Labbe, P. A. Oesch, M. Trenti, C. M. Carollo, P. G. van Dokkum, M. Franx, M. Stiavelli, V. González, D. Magee, and L. Bradley. 2011. A candidate redshift z~10 galaxy and rapid changes in that population at an age of 500Myr. *Nature* 469:504–507.

Bouwens, R. J., G. D. Illingworth, P. A. Oesch, M. Trenti, I. Labbé, L. Bradley, M. Carollo, P. G. van Dokkum, V. Gonzalez, B. Holwerda, M. Franx, L. Spitler, R. Smit, and D. Magee. 2015. UV Luminosity Functions at Redshifts z 4 to z 10: 10,000 Galaxies from HST Legacy Fields. *the Astrophysical Journal* 803:34.

Bouwens, R. J., P. A. Oesch, I. Labbé, G. D. Illingworth, G. G. Fazio, D. Coe, B. Holwerda, R. Smit, M. Stefanon, P. G. van Dokkum, M. Trenti, M. L. N. Ashby, J. S. Huang, L. Spitler, C. Straatman, L. Bradley, and D. Magee. 2016. The Bright End of the z 9 and z 10 UV Luminosity Functions Using All Five CANDELS Fields*. *the Astrophysical Journal* 830:67.

Bromm, Volker, Paolo S. Coppi, and Richard B. Larson. 2002. The Formation of the First Stars. I. The Primordial Star-forming Cloud. *the Astrophysical Journal* 564:23–51.

Chiaki, Gen, Naoki Yoshida, and Shingo Hirano. 2016. Gravitational collapse and the thermal evolution of low-metallicity gas clouds in the early Universe. *Monthly Notices of the Royal Astronomical Society* 463:2781–2798.

Clark, Paul C., Simon C. O. Glover, Ralf S. Klessen, and Volker Bromm. 2011. Gravitational Fragmentation in Turbulent Primordial Gas and the Initial Mass Function of Population III Stars. *the Astrophysical Journal* 727:110.

Coe, Dan, Adi Zitrin, Mauricio Carrasco, Xinwen Shu, Wei Zheng, Marc Postman, Larry Bradley, Anton Koekemoer, Rychard Bouwens, Tom Broadhurst, Anna Monna, Ole Host, Leonidas A. Moustakas, Holland Ford, John Moustakas, Arjen van der Wel, Megan Donahue, Steven A. Rodney, Narciso Benítez, Stephanie Jouvel, Stella Seitz, Daniel D. Kelson, and Piero Rosati. 2013. CLASH: Three Strongly Lensed Images of a Candidate z $\approx$ 11 Galaxy. *the Astrophysical Journal* 762:32.

Crutcher, Richard M. 1999. Magnetic Fields in Molecular Clouds: Observations Confront Theory. *the Astrophysical Journal* 520:706–713.

Crutcher, Richard M., Benjamin Wandelt, Carl Heiles, Edith Falgarone, and Thomas H. Troland. 2010. Magnetic Fields in Interstellar Clouds from Zeeman

Observations: Inference of Total Field Strengths by Bayesian Analysis. *the Astrophysical Journal* 725:466–479.

Duquennoy, A., and M. Mayor. 1991. Multiplicity among solar-type stars in the solar neighbourhood. II - Distribution of the orbital elements in an unbiased sample. *Astronomy & Astrophysics* 500:337–376.

Ebert, R. 1955. Über die Verdichtung von H I-Gebieten. Mit 5 Textabbildungen. *Z. Astrophys.* 37:217.

Ellis, Richard S., Ross J. McLure, James S. Dunlop, Brant E. Robertson, Yoshiaki Ono, Matthew A. Schenker, Anton Koekemoer, Rebecca A. A. Bowler, Masami Ouchi, Alexander B. Rogers, Emma Curtis-Lake, Evan Schneider, Stephane Charlot, Daniel P. Stark, Steven R. Furlanetto, and Michele Cirasuolo. 2013. The Abundance of Star-forming Galaxies in the Redshift Range 8.5-12: New Results from the 2012 Hubble Ultra Deep Field Campaign. *The Astrophysical Journal Letters* 763:L7.

Falgarone, E., M. A. Zwaan, B. Godard, E. Bergin, R. J. Ivison, P. M. Andreani, F. Bournaud, R. S. Bussmann, D. Elbaz, A. Omont, I. Oteo, and F. Walter. 2017. Large turbulent reservoirs of cold molecular gas around high-redshift starburst galaxies. *Nature* 548:430–433.

Galli, Daniele, and Francesco Palla. 1998. The chemistry of the early Universe. *Astronomy & Astrophysics* 335:403–420.

Goodman, A. A., P. J. Benson, G. A. Fuller, and P. C. Myers. 1993. Dense Cores in Dark Clouds. VIII. Velocity Gradients. *the Astrophysical Journal* 406:528.

Hanawa, Tomoyuki, and Tomoaki Matsumoto. 2000. Stability of a Dynamically Collapsing Gas Sphere. *Publications of the Astronomical Society of Japan* 52:241.

Heger, A., and S. E. Woosley. 2002. The Nucleosynthetic Signature of Population III. *the Astrophysical Journal* 567:532–543.

Heiles, C., and R. Crutcher. 2005. *Magnetic Fields in Diffuse HI and Molecular Clouds*, volume 664, 137.

Higuchi, Koki, Masahiro N. Machida, and Hajime Susa. 2018. Evolution of magnetic fields in collapsing star-forming clouds under different environments. *Monthly Notices of the Royal Astronomical Society* 475:3331–3347.

Higuchi, Koki, Masahiro N. Machida, and Hajime Susa. 2019. Driving conditions of protostellar outflows in different star-forming environments. *Monthly Notices of the Royal Astronomical Society* 486:3741–3754.

Hirano, S., T. Hosokawa, N. Yoshida, K. Omukai, and H. W. Yorke. 2015. Primordial star formation under the influence of far ultraviolet radiation: 1540 cosmological haloes and the stellar mass distribution. *Monthly Notices of the Royal Astronomical Society* 448:568–587.

Hirano, Shingo, Takashi Hosokawa, Naoki Yoshida, Hideyuki Umeda, Kazuyuki Omukai, Gen Chiaki, and Harold W. Yorke. 2014. One Hundred First Stars: Protostellar Evolution and the Final Masses. *the Astrophysical Journal* 781:60.

Hosokawa, Takashi, Shingo Hirano, Rolf Kuiper, Harold W. Yorke, Kazuyuki Omukai, and Naoki Yoshida. 2016. Formation of Massive Primordial Stars: Intermittent UV Feedback with Episodic Mass Accretion. *the Astrophysical Journal* 824:119.

Hosokawa, Takashi, Kazuyuki Omukai, Naoki Yoshida, and Harold W. Yorke. 2011. Protostellar Feedback Halts the Growth of the First Stars in the Universe. *Science* 334:1250.

Hosokawa, Takashi, Naoki Yoshida, Kazuyuki Omukai, and Harold W. Yorke. 2012. Protostellar Feedback and Final Mass of the Second-generation Primordial Stars. *The Astrophysical Journal Letters* 760:L37.

Ishigaki, Masafumi, Ryota Kawamata, Masami Ouchi, Masamune Oguri, Kazuhiro Shimasaku, and Yoshiaki Ono. 2015. Hubble Frontier Fields First Complete Cluster Data: Faint Galaxies at z ~5-10 for UV Luminosity Functions and Cosmic Reionization. *the Astrophysical Journal* 799:12.

Kinugawa, Tomoya, Takashi Nakamura, and Hiroyuki Nakano. 2017. The possible existence of Pop III NS-BH binary and its detectability. *Progress of Theoretical and Experimental Physics* 2017:021E01.

Lai, Dong. 2000. Global Nonradial Instabilities of Dynamically Collapsing Gas Spheres. *the Astrophysical Journal* 540:946–961.

Lam, Daniel, Rychard J. Bouwens, Dan Coe, Adi Zitrin, Christopher Barber, Ivo Labbe, Themiya Nanayakkara, Megan Donahue, Renske Smit, Xinwen Shu, Ranga-Ram Chary, John Moustakas, Mario Nonino, Daniel D. Kelson, Tom Broadhurst, Larry Bradley, Mauricio Carrasco, and Piero Rosati. 2019. Detection of a Lensed z≈11 Galaxy in the Rest-Optical with Spitzer/IRAC and the Inferred SFR, Stellar Mass, and Physical Size. *arXiv e-prints* arXiv:1903.08177.

Latif, Muhammad A., and Sadegh Khochfar. 2019. UV regulated star formation in high-redshift galaxies. *Monthly Notices of the Royal Astronomical Society* 490:2706–2716.

Lucatello, Sara, Stelios Tsangarides, Timothy C. Beers, Eugenio Carretta, Raffaele G. Gratton, and Sean G. Ryan. 2005. The Binary Frequency Among Carbon-enhanced, s-Process-rich, Metal-poor Stars. *the Astrophysical Journal* 625:825–832.

Machida, Masahiro N., and Takashi Hosokawa. 2013. Evolution of protostellar outflow around low-mass protostar. *Monthly Notices of the Royal Astronomical Society* 431:1719–1744.

Machida, Masahiro N., Shu-ichiro Inutsuka, and Tomoaki Matsumoto. 2007. Magnetic Fields and Rotations of Protostars. *the Astrophysical Journal* 670:1198–1213.

Machida, Masahiro N., Tomoaki Matsumoto, Tomoyuki Hanawa, and Kohji Tomisaka. 2005. Collapse and fragmentation of rotating magnetized clouds - II. Binary formation and fragmentation of first cores. *Monthly Notices of the Royal Astronomical Society* 362:382–402.

Machida, Masahiro N., Tomoaki Matsumoto, and Shu-ichiro Inutsuka. 2008a. Magnetohydrodynamics of Population III Star Formation. *the Astrophysical Journal* 685:690–704.

Machida, Masahiro N., Kazuyuki Omukai, Tomoaki Matsumoto, and Shu-ichiro Inutsuka. 2008b. Conditions for the Formation of First-Star Binaries. *the Astrophysical Journal* 677:813–827.

Machida, Masahiro N., Kohji Tomisaka, and Tomoaki Matsumoto. 2004. First MHD simulation of collapse and fragmentation of magnetized molecular cloud cores. *Monthly Notices of the Royal Astronomical Society* 348:L1–L5.

Mao, S. A., C. Carilli, B. M. Gaensler, O. Wucknitz, C. Keeton, A. Basu, R. Beck, P. P. Kronberg, and E. Zweibel. 2017. Detection of microgauss coherent magnetic fields in a galaxy five billion years ago. *Nature Astronomy* 1:621–626.

Matsumoto, Tomoaki, and Tomoyuki Hanawa. 1999. Bar and Disk Formation in Gravitationally Collapsing Clouds: Implications for Binary Formation. *the Astrophysical Journal* 521:659–670.

Matsumoto, Tomoaki, and Kohji Tomisaka. 2004. Directions of Outflows, Disks, Magnetic Fields, and Rotation of Young Stellar Objects in Collapsing Molecular Cloud Cores. *the Astrophysical Journal* 616:266–282.

McClure, Robert D., and A. W. Woodsworth. 1990. The Binary Nature of the Barium and CH Stars. III. Orbital Parameters. *the Astrophysical Journal* 352:709.

McLure, R. J., J. S. Dunlop, R. A. A. Bowler, E. Curtis-Lake, M. Schenker, R. S. Ellis, B. E. Robertson, A. M. Koekemoer, A. B. Rogers, Y. Ono, M. Ouchi, S. Charlot, V. Wild, D. P. Stark, S. R. Furlanetto, M. Cirasuolo, and T. A. Targett. 2013. A new multifield determination of the galaxy luminosity function at z = 7-9 incorporating the 2012 Hubble Ultra-Deep Field imaging. *Monthly Notices of the Royal Astronomical Society* 432:2696–2716.

Nakamura, Fumitaka, and Masayuki Umemura. 2002. The Stellar Initial Mass Function in Primordial Galaxies. *the Astrophysical Journal* 569:549–557.

Nakano, T., and T. Nakamura. 1978. Gravitational Instability of Magnetized Gaseous Disks 6. *Publications of the Astronomical Society of Japan* 30:671–680.

Oesch, P. A., G. Brammer, P. G. van Dokkum, G. D. Illingworth, R. J. Bouwens, I. Labbé, M. Franx, I. Momcheva, M. L. N. Ashby, G. G. Fazio, V. Gonzalez, B. Holden, D. Magee, R. E. Skelton, R. Smit, L. R. Spitler, M. Trenti, and S. P. Willner. 2016. A Remarkably Luminous Galaxy at z=11.1 Measured with Hubble Space Telescope Grism Spectroscopy. *the Astrophysical Journal* 819:129.

Omukai, K., T. Tsuribe, R. Schneider, and A. Ferrara. 2005. Thermal and Fragmentation Properties of Star-forming Clouds in Low-Metallicity Environments. *the Astrophysical Journal* 626:627–643.

Palla, F., E. E. Salpeter, and S. W. Stahler. 1983. Primordial star formation - The role of molecular hydrogen. *the Astrophysical Journal* 271:632–641.

Price, Daniel J., and Matthew R. Bate. 2007. The impact of magnetic fields on single and binary star formation. *Monthly Notices of the Royal Astronomical Society* 377:77–90.

Schleicher, D. R. G., R. Banerjee, S. Sur, T. G. Arshakian, R. S. Klessen, R. Beck, and M. Spaans. 2010. Small-scale dynamo action during the formation of the first stars and galaxies. I. The ideal MHD limit. *Astronomy & Astrophysics* 522:A115.

Stanway, Elizabeth R., Andrew J. Bunker, and Richard G. McMahon. 2003. Lyman break galaxies and the star formation rate of the Universe at z˜6. *Monthly Notices of the Royal Astronomical Society* 342:439–445.

Steidel, Charles C., Mauro Giavalisco, Max Pettini, Mark Dickinson, and Kurt L. Adelberger. 1996. Spectroscopic Confirmation of a Population of Normal Star-forming Galaxies at Redshifts Z > 3. *The Astrophysical Journal Letters* 462:L17.

Steidel, Charles C., Alice E. Shapley, Max Pettini, Kurt L. Adelberger, Dawn K. Erb, Naveen A. Reddy, and Matthew P. Hunt. 2004. A SURVEY OF STAR-FORMING GALAXIES IN THE 1.4 ¡ z ¡ 2.5 REDSHIFT DESERT: OVERVIEW. *the Astrophysical Journal* 604:534–550.

Susa, Hajime, Kentaro Doi, and Kazuyuki Omukai. 2015. Dissipation of Magnetic Fields in Star-forming Clouds with Different Metallicities. *the Astrophysical Journal* 801:13.

Susa, Hajime, Kenji Hasegawa, and Nozomu Tominaga. 2014. The Mass Spectrum of the First Stars. *the Astrophysical Journal* 792:32.

Tacconi, L. J., R. Genzel, I. Smail, R. Neri, S. C. Chapman, R. J. Ivison, A. Blain, P. Cox, A. Omont, F. Bertoldi, T. Greve, N. M. Förster Schreiber, S. Genel, D. Lutz, A. M. Swinbank, A. E. Shapley, D. K. Erb, A. Cimatti, E. Daddi, and A. J. Baker. 2008. Submillimeter Galaxies at z ~2: Evidence for Major Mergers and Constraints on Lifetimes, IMF, and CO-H_2 Conversion Factor. *the Astrophysical Journal* 680:246–262.

Tomida, Kengo, Satoshi Okuzumi, and Masahiro N. Machida. 2015. Radiation Magnetohydrodynamic Simulations of Protostellar Collapse: Nonideal Magnetohydrodynamic Effects and Early Formation of Circumstellar Disks. *the Astrophysical Journal* 801:117.

Tomisaka, Kohji. 2000. The Evolution of the Angular Momentum Distribution during Star Formation. *The Astrophysical Journal Letters* 528:L41–L44.

Truelove, J. Kelly, Richard I. Klein, Christopher F. McKee, II Holliman, John H., Louis H. Howell, and Jeffrey A. Greenough. 1997. The Jeans Condition: A New Constraint on Spatial Resolution in Simulations of Isothermal Self-gravitational Hydrodynamics. *The Astrophysical Journal Letters* 489:L179–L183.

Turk, Matthew J., Tom Abel, and Brian O'Shea. 2009. The Formation of Population III Binaries from Cosmological Initial Conditions. *Science* 325:601.